Materials Advances

Accepted Manuscript

This article can be cited before page numbers have been issued, to do this please use: R. Shikuku, M. A. Hasnat and M. N. Khan, *Mater. Adv.*, 2026, DOI: 10.1039/D5MA01301A.

ROYAL SOCIETY OF CHEMISTRY

rsc.li/materials-advances

View Article Online
DOI: 10.1039/D5MA01301A

Engineered CuO-GO Reinforced PVA/CS Electrospun Nanofibers with Enhanced Physicochemical, Hemocompatible, and Wound Healing Performance

*Raymond Shikuku, Mohammed Abul Hasnat, and M. Nuruzzaman Khan**

Department of Applied Chemistry and Chemical Engineering, Faculty of Engineering and Technology, University of Dhaka, Dhaka-1000, Bangladesh

Abstract:

Wound management is a critical aspect of healthcare that demands the development of effective and innovative dressing materials. Yet, many conventional wound dressings exhibit significant limitations, such as poor healing efficacy, potential cytotoxicity, inadequate moisture retention, and insufficient mechanical strength, which collectively hinder optimal healing outcomes. To overcome these limitations, we developed a biodegradable nanofibrous mat composed of polyvinyl alcohol (PVA) and chitosan (CS) through electrospinning process. The resulting mat features a three-dimensional (3D) interconnected porous structure that offers a high surface-area-to-volume ratio and enhanced porosity, favorable for wound healing applications. To impart bioactivity, a copper oxide/graphene oxide (1:1 ratio) nanostructure was incorporated into the nanofibrous matrix. The CuO-GO composite was formed via ex-situ ultrasonic mixing, yielding spherical CuO NPs (~49 nm) uniformly distributed on GO nanosheets, as confirmed by transmission electron microscopy (TEM). The CuO-GO-embedded PVA/CS nanofibrous mats were thermally crosslinked at 120 °C for 80 min to improve structural integrity. Fourier-transform infrared spectroscopy (FTIR) confirmed successful incorporation of the nanocomposite, while scanning electron microscopy (SEM) revealed uniform fiber morphology with diameters ranging from 116

View Article Online
DOI: 10.1039/D5MA01301A

to 290 nm, depending on CuO-GO loading (0–2 wt%). Mechanical testing demonstrated that CuO-GO incorporation enhanced tensile strength but decreased ductility. Additionally, the crosslinked mats showed reduced hydrophilicity and controlled degradation rates matching the wound healing process. Cytotoxicity assessments and hemocompatibility analysis determined the biocompatible concentration range of CuO-GO into the mat, guiding safe application dosages. In *in vivo* full-thickness wound healing studies, mats containing 2 wt% CuO-GO achieved over 95% of wound contraction within 14 days, significantly go beyond control samples. These findings accentuate the potential of the CuO–GO-embedded PVA/CS nanofibrous mat as an effective therapeutic wound dressing that promotes enhanced skin regeneration, while its controlled degradation ensures the material breaks down soundly in line with the healing process.

Keywords: Chitosan, wound healing, CuO-GO nanostructure, electrospun nanofibers, histopathology

* To whom correspondence should be addressed.

E-mail: mnuruzzaman.khan@du.ac.bd; Tel: (+880)-1717057445

View Article Online
DOI: 10.1039/D5MA01301A

1. INTRODUCTION

A wound is a disruption in the defensive function of the skin. Wounds are classified as either chronic or acute based on the duration of their healing process. Acute wounds classically follow a predictable healing sequence: hemostasis, inflammation, proliferation, and remodeling, thereby healing at a predictable time, generally 3 weeks [1]. On the other hand, chronic wounds, often associated with conditions such as diabetes, vascular diseases, or pressure injuries, and vascular diseases, frequently linger in the inflammatory stage, leading to prolonged healing times duration, heightened infection risks, increased high morbidity, and even mortality [2]. Therefore, the development of ideal wound care materials to accelerate chronic wound healing process is a major concern.

An ideal wound healing material should be designed with active biomaterial materials that can reduce inflammation and simultaneously promote early cell proliferation to regenerate damaged tissues [1]. Recently, bio-conjugated copper nanomaterials have been used in skin tissue engineering. Among various nanomaterials, copper oxide (CuO) and graphene oxide (GO) have been studied as an active material for tissue regeneration. Cu has been shown to stimulate the release of platelet-derived growth factor (PDGF) [2], and prostaglandins during the hemostatic phase and the inflammatory phase, respectively [3]. It also stimulates the production of fibroblast growth factors (FGF), nerve growth factor, angiotensin II, and transforming growth factor beta (TGF-β), which helps accelerate wound healing [4]. Moreover, Copper promotes the expression of Cu-dependent enzymes and polysaccharide molecules, including lysyl oxidase, nanofibrous matrix metalloproteinases, glycosaminoglycans, and small proteoglycans that play vital roles in extracellular matrix remodeling, cellular proliferation, re-epithelialization, and the migration of skin and stem cells [5].

View Article Online
DOI: 10.1039/D5MA01301A

Similarly, graphene oxide, a carbon-based material, is characterized by its exceptionally high surface area, superior thermal conductivity, significant drug-loading capacity, desirable biocompatibility and biodegradability. It has been extensively reported to promote cellular adhesion, proliferation, and differentiation [6]. In addition, GO nanosheets exhibit both wound-healing efficacy and antibacterial properties, notably against Staphylococcus aureus [7].

Furthermore, the synergistic interaction between CuO NPs and GO sheets in facilitating wound repair presents a compelling area of research. Due to its intrinsic hydrophilicity, GO displays excellent dispersion in aqueous media, minimal cytotoxicity, and enhanced biocompatibility, making it a viable candidate for medical utilizations. GO is formed through altering the chemical composition of graphene. During the oxidation process, hydroxyl (-OH), carboxyl (-COOH), and epoxide (C-O-C) functional groups are introduced onto both the basal planes and edges of the graphene sheets.

To ensure uniform and efficient, delivery of the CuO-GO nanocomposite at the wound site, we designed an electrospun nanofibrous mat using poly(vinyl alcohol) (PVA) and chitosan (CS) as the carrier matrix. Nanofiber mats are ideal for wound care due to their high surface area-to-volume ratio, high porosity, and high aspect ratio, which enhance cell attachment and cell migration [8]. Their high porosity can also create a moist wound environment by absorbing exudates. It is widely recognized that a moist wound is advantageous in the healing process of acute and chronic wounds as it supports epidermal cell migration and increases the rate of re-epithelialization and angiogenesis.

Chitosan, derived from chitin, is widely used in the fabrication of wound healing scaffolds because it is biocompatible, biodegradable, and bioactive, promoting hemostasis and tissue regeneration [9]. However, its high viscosity and polycationic nature make the electrospinning process

View Article Online
DOI: 10.1039/D5MA01301A

challenging. Blending chitosan and synthetic polymers such as PVA improves spinning conditions [10]. PVA is a water-soluble, non-ionic polymer approved by the FDA. It is generally recognized as safe to use in medical applications due to its biocompatibility, availability, and stability. It has been shown to reduce repulsive interactions of chitosan chains, enhancing molecular interactions.

Despite this, the structural integrity of PVA/CS nanofibrous mat is often poor. To address this, electrospun nanofibrous mats can be cross-linked through thermal treatment, UV irradiation, or chemical cross-linkers such as glutaraldehyde (GTA), which efficiently cross-link without compromising structural integrity [11].

Electrospun nanofibrous mats containing copper-based nanomaterials have attracted growing attention for wound healing due to their broad-spectrum antimicrobial activity and ability to modulate cellular processes involved in tissue regeneration. Sandra *et al.* [12] incorporated CuO nanoparticles into PVA/chitosan (PVA/CS) nanofibers, and found enhanced antioxidant activity, improved cell viability (MTT assay), and accelerated wound closure along with antibacterial efficacy. Although promising, the study was limited by the absence of *in vivo* wound healing study. In another study, Lemraski *et al.* [13] fabricated a bilayer wound dressing consisting of an outer PVA/CS/CuNPs layer and an inner polyvinylpyrrolidone (PVP) layer. This study results demonstrated that copper could modulate key biological processes, including fibroblast and keratinocyte proliferation, epithelialization, angiogenesis, and collagen synthesis, factors critical for efficient wound repair. Moreover, graphene oxide (GO) nanosheets have emerged as a multifunctional carbon nanomaterial due to their high surface area, reactive oxygen species (ROS) scavenging ability, and capacity to enhance cell proliferation and migration. Heidari *et al.* [14], developed electrospun nanofibers composed of polycaprolactone (PCL), gelatin, and GO for nerve tissue engineering. The *in vitro* studies demonstrated enhanced cell adhesion, migration, and

View Article Online
DOI: 10.1039/D5MA01301A

proliferation, indicating that the PCL/gelatin/GO scaffolds provided a supportive microenvironment without prompting cytotoxic effects. However, the study lacked *in vivo* validation. Similarly, Dubey *et al.* [15] synthesized a PEGylated GO-based nanocomposite embedded in PVA/CS nanofibers for use in wound dressing. The results showed that GO improves the mechanical and antibacterial, the study lacked *in vivo* validation. In a related study, chitosan/gelatin nanofibers reinforced with GO nanosheets showed significantly improved cell migration at 24 and 48 h compared to non-reinforced scaffolds, suggesting GO's positive influence on cellular motility and scaffold–cell interactions [16]. Studies have reported that GO, either alone or in combination with metal nanoparticles, can further expand wound healing outcomes due to its favorable physicochemical and biological properties[17].

Therefore, CuO-GO NCs were incorporated into the PVA/CS polymer solution, and the solution was electrospun to produce a biodegradable CuO-GO embedded PVA/CS nanofibrous mat. The nanofibrous mat was further crosslinked through thermal treatment in an oven at 120°C for 80 min to enhance the fiber's stability in an aqueous medium, thereby balancing the fiber degradation to the rate of wound healing. To the best of our knowledge, a thorough investigation into CuO-GO NCs loaded into a thermally crosslinked PVA/CS nanofibrous mat, the outcome of their loading concentration on cytotoxicity of cells, and *in vivo* wound healing has not been explored. Therefore, in this study, several tests were conducted to analyze the fabricated nanofibrous mat, including scanning electron microscopy (SEM), differential scanning calorimetry (DSC), Fourier transform infrared (FTIR) spectroscopy, and a universal testing machine (UTM) for mechanical property analyses. Furthermore, the water contact angle, swelling ratio, and degradation of the nanofibrous mats were examined. The potential of these nanofibrous mats as wound dressings was further

View Article Online
DOI: 10.1039/D5MA01301A

assessed through *in vitro* cytotoxicity tests, hemolysis assay and blood clot index analysis and *in vivo* wound healing studies.

2. MATERIALS AND METHODS

2.1. Materials

Low-molecular-weight chitosan (Sigma-Aldrich, Germany, DDA >75%) was purchased from Sisco Research Laboratories, India. Poly (vinyl alcohol) (Research Lab Fine Chem Industries, India; Mw = 115,000, degree of hydrolysis 98%), and cupric sulfate pentahydrate ($CuSO_4 \cdot 5H_2O$; Merck, India) were purchased. Graphite powder, potassium permanganate ($KMnO_4$, 99.0%), sodium nitrate ($NaNO_3$), hydrogen peroxide (H_2O_2), sulfuric acid (H_2SO_4, 99.0%), nitric acid (HNO_3), hydrochloric acid (HCl), phosphate-buffered saline (PBS), sodium hydroxide (NaOH), and glacial acetic acid (CH_3COOH) were purchased from Sigma-Aldrich, Germany. All chemicals were used without further purification.

2.2. Preparation of CuO NPs

The CS stabilized CuO NPs were synthesized according to the method of T. J method [18]. Firstly, a stock solution of CS was prepared by dissolving 1.5 g of CS in 100 mL containing 1.5% (v/v) acetic acid double-distilled water at 60 °C. Concurrently, 5.0 g of $CuSO_4 \cdot 5H_2O$ was dissolved in 100 mL of double-distilled water. Next, 20 mL of the as prepared CS solution was slowly added to the copper sulfate solution, and the mixture was vigorously stirred for 30 min to ensure homogeneity. The temperature was raised to 85 °C, and the reaction was allowed to progress for another 45 min. Using a dilute sodium hydroxide solution (0.625 M), the solution pH was adjusted to 9, and a dense blue colour was noted as the precipitate formed. Finally, the precipitate was separated by centrifugation at 8000 rpm for 20 min. Distilled water was used to wash out the

View Article Online
DOI: 10.1039/D5MA01301A

unreacted chemicals and other contaminants. The obtained solids were dried in a hot air oven set at 60 °C overnight and then calcined at 600 °C for 4h. The experimental procedure is shown in **Scheme 1a.**

2.3 Preparation of GO nanosheets

The preparation procedure of the GO nanosheets followed the modified hammer method [19]. Briefly, a 75 mL of acid mixture made up of conc. Sulfuric acid (H_2SO_4) and nitric acid (HNO_3) at a ratio of 3:1 was placed in a round-bottomed flask. As a safety measure, the flask was immersed in a cold bath at 0 °C. To this mixture, 3.0 g of graphite powder was added and dispersed with vigorous stirring using a magnetic stirrer. Then 9 g of $KMnO_4$ and 1.5 g of $NaNO_3$ were slowly added while avoiding rapid temperature rise above 20 °C, and the mixture was stirred for an additional 2 h. After removing the water bath, the reaction mixture was allowed to stir overnight, resulting in the formation of a thick brown paste.

Next, 150 mL of deionized (DI) water was added, and a violent effervescence was noted as the temperature rose above 90 °C. The reaction was allowed to progress for another 15 min, and 420 mL of distilled water was added, followed by adding 80mL of 30% hydrogen peroxide. At this point, the solution color turned bright yellow. Then, 200 mL of 5% HCl was used to remove the manganese ions from graphene oxide. Finally, the solution was filtered, and the filtrate was thoroughly washed to neutralize the prepared GO to pH 7.0. The washing process was conducted for 30 days as the suspended particles were allowed to agglomerate and settle via gravity and eventually centrifuged. The obtained GO was dried for 18 h at 60 °C in a hot air oven and stored in a desiccator for characterization and application. The GO synthesis route is illustrated in **Scheme 1b**.

View Article Online
DOI: 10.1039/D5MA01301A

2.4 Ultrasound-assisted synthesis of CuO-GO NC.

The nanocomposite was synthesized following our previously reported methods [10]. Briefly, 0.5 g of GO and 0.5 g of CuO were concurrently dispersed in 50 mL of distilled water. Then it was ultrasonicated for 5 h at 80 °C. Next, the composite was separated via centrifugation at 2000 rpm for 20 min. Finally, the as prepared nanocomposite was dried at 100 °C in a hot air oven and stored in a desiccator before application in preparing the functionalized nanofiber scaffold. The synthesis route is shown in **Scheme 1c**.

2.5 Electrospinning process

2.5.1 Preparation of polymer solution

First, 2 g of PVA beads were added to 20 mL of DI water-acetic acid solution (20% acetic acid), and the temperature of the solution was maintained at 80 °C for 1h with constant agitation to ensure total dissolution. The mixture was then settled out to room temperature and ultrasonicated for 1h to remove air bubbles. 0.2g of CS powder was added to the PVA solution and kept stirring overnight. The required amounts of CuO-GO (0.75%, 1%, 1.5%, and 2% by weight) were dispersed in deionized (DI) water and ultrasonicated for 1 h to obtain a homogeneous and uniform dispersion of CuO-GO. It was then added to the as prepared PVA/CS electrospinimg solution and stirred continuously for 2 h. Later, the mixture was further ultrasonicated for an additional 1 h to ensure thorough mixing and uniformity.

2.5.2 Viscosity and electrical conductivity of polymeric solution

The PVA/CS and CuO-GO loaded PVA/CS solutions were characterized using a rotational viscometer (Elcometer 2300, USA) equipped with a temperature probe. The rotary viscometer measures the viscosity of liquids according to ISO 2555. The solutions were assessed at

View Article Online
DOI: 10.1039/D5MA01301A

temperature of 25 °C at a shear rate of between 3 and 22 s^{-1}. The conductivity of the polymeric solutions was evaluated with a handheld portable conductivity meter (Hanna HI 8033, Italy) and a conductivity probe sensor (4-Ring Conductivity Probe - HI76301, Hanna, Italy). All the tests were conducted in triplicate.

2.5.3 Fabrication of electrospun nanofiber

The electrospinning process, as shown in Scheme 1e, was designed by first loading 5 mL of CuO-GO incorporated PVA/CS nanocomposite solution into a syringe with a metallic needle. The syringe was then mounted on the pump. A rotating cylindrical collector was covered with aluminum foil and positioned directly in front of the needle tip; the needle-to-collector distance was maintained at 15cm. Next, the flow rate and voltage were set at 0.9 mL/h and 19 kV, respectively. The obtained nanofiber mats were then subjected to thermal crosslinking at 120 °C for 80 min (40 min on each side), and the as-obtained nanofibrous mat was stored in a desiccator for further characterization and applications.

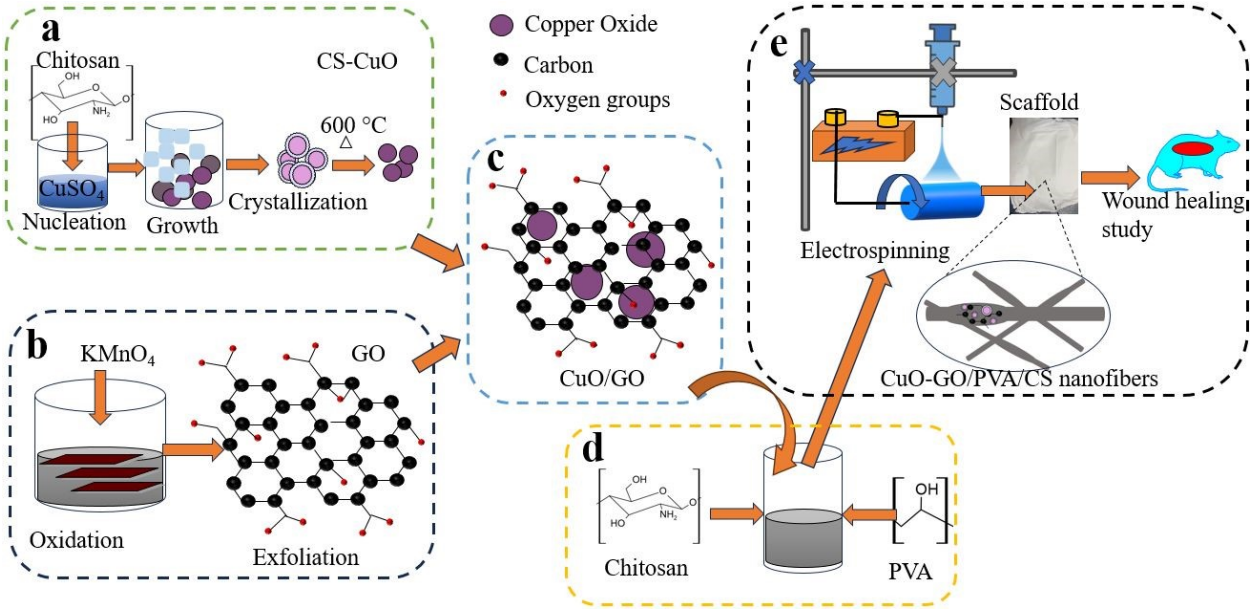

View Article Online
DOI: 10.1039/D5MA01301A

Scheme 1. Synthesis process of (a) CuO, (b) GO, (c) CuO-GO NC, (d) CuO-GO loaded PVA/CS spinning solution, and (e) Electrospinning, characterization, and in vivo wound healing study. process.

2.6 Fourier Transformed Infrared (ATR-FTIR) Spectroscopy

The chemical structures of the as-prepared GO, CuO, CuO-GO NCs, and CuO-GO loaded PVA/CS electrospun fibrous mats were characterized using Fourier-transform infrared (FTIR) spectroscopy (IRPrestige-21, Shimadzu, Japan). The FTIR spectra were recorded in the range of 4000–500 cm^{-1} with a resolution of 2 cm^{-1}, averaging 128 scans per sample.

2.7 X-ray Diffraction (XRD)

The crystal structures of GO, CuO, and CuO-GO NPs were studied by an X-ray diffractometer (Rigaku Ultima IV, Japan) using Cu-K radiation with a wavelength of 0.15418 nm. Data were collected in the 2θ range of 5−80°, with a 0.02° step and a counting time of 1s per step.

2.8 Scanning Electron Microscopy (SEM) and EDX

A scanning electron microscope, Zeiss sigma VP300 FE-SEM, Germany, was used to observe the surface morphology and topography of the CuO-GO loaded PVA/CS nanofibrous mat. The voltage was 10 kV. The samples were coated with platinum using an auto-coater through the ion-sputtering process. Fiber diameters were determined from SEM images using ImageJ software (version 1.53t), and the average standard deviation was used to represent the data. From the high-resolution SEM images at 20 kV of the nanofiber surface, energy-dispersive X-ray (EDX) mapping was performed to determine the different elements present in the nanofiber.

2.9 TEM analysis of electrospun Nanofibrous mats.

View Article Online
DOI: 10.1039/D5MA01301A

The nanofibers were analyzed by transmission electron microscopy (Talos F200×G2 TEM (Czech Republic) at 10 kV. Sample preparation was done by electrospinning a thin layer of fibers onto a holey carbon-coated copper grid for TEM image analysis.

2.10 Differential Scanning Calorimetry (DSC)

Before the DSC analysis, the electrospun nanofibrous mats were conditioned in a desiccator for 48 h at ambient conditions. The thermal behavior of the electrospun nanofiber mat was assessed using differential scanning calorimetry (STA 449 F5 Jupiter system NETZSCH, Germany). The experimental setup included an aluminum cell and sample heating in a temperature range of 30 - 300 ºC with a heating rate of 10 ºC min^{-1} and nitrogen gas flux of 20 mL min^{-1}. The latent heat of melting (ΔHm) values was calculated based on equation 1.

$$\Delta H_m = \int_{T_{start}}^{T_{end}} \frac{dQ}{dt} dt \quad \text{... (1)}$$

Here ΔH is specific enthalpy (J/g), T_{end} is time of endotherm start (s), T_{start} is time of endotherm end (s), dQ/dt is normalized heat flow (W/g), dt is integration time (s)

The degree of crystallinity (X_c) of the nanofibers was calculated according to equation 2.

$$X_C(\%) = \frac{\Delta H_f}{(w_{PVA})\Delta H_f^o} * 100 \quad \text{... (2)}$$

where ΔH_f^o is the enthalpy of fusion of 100% crystalline PVA, ΔH_f is the enthalpy of fusion of the sample; and w_{PVA} is the mass fraction of PVA used in the mixture [20].

2.11 Mechanical Properties

The mechanical properties of the CuO-GO embedded PVA/CS nanofibrous mats were evaluated using an electromechanical testing instrument (Shenzhen Wance ETM 501, China) in accordance

View Article Online
DOI: 10.1039/D5MA01301A

with the ASTM D882 standard [21]. Test specimens with a width of 7 mm and a gauge length of 12 mm were examined using a 10 N load cell at a crosshead speed of 2 mm/min. Each electrospun mat was tested in triplicate to ensure reproducibility.

2.12 Porosity

Furthermore, the porosity of the nanofibrous mat was measured based on Archimedes' method [22]. The as-prepared mat with 2 cm × 2 cm dimensions were conditioned for 1 h in an oven at 60 °C. After that, the porosity was determined by soaking the mat in ethanol, giving the liquid-accessible pores. The mats were then subjected to centrifugation at 6000 rpm for 10 min, which allowed the ethanol to fill their pores. The weight of the mat after being soaked in ethanol was recorded (M_s). The volume of the ethanol filling the pores was calculated as V_p, while the volume taken up by the mat was V_s. The bulk density of PVA, CS, and ethanol is 1.19, 1.21, and 0.79 g/cm^3, respectively [23][24] . The porosity was determined using equations 3, 4, and 5, where $\rho_{ethanol}$ and $\rho_{PVA/CS}$ are the densities of ethanol and PVA/CS composite, respectively. An average of three measurements was taken for each sample.

$$Porosity\% = \left(\frac{V_p}{V_p - V_s}\right)100 \quad \text{... (3)}$$

$$V_p = \left(\frac{M_s - M_d}{\rho_{Ethanol}}\right) \quad \text{... (4)}$$

$$V_p = \left(\frac{M_d}{\rho_{PVA/CS}}\right) \quad \text{... (5)}$$

View Article Online
DOI: 10.1039/D5MA01301A

2.13 Wetting Property

The wetting property of the nanofibrous mat was determined by the static contact angle analysis using the sessile drop method DMe-211, Kyowa Interface Science Co. Ltd. Japan) at room temperature. The experimental setup consisted of a vertically mounted clamp designed to hold a syringe filled with deionized water in a fixed position. On one side of the apparatus, a high-intensity light source was aligned to provide focused illumination, while a camera was positioned directly opposite to capture the transmitted optical images. Both devices were interfaced with a computer system for synchronized image acquisition and data recording. At precisely 5 seconds after the deposition of each water droplet onto the nanofibrous mat surface, optical images were captured to monitor the initial absorption behavior of the mat using DROPimage software (n = 3).

2.14 Swelling and degradation Analyses

The swelling ratios of the nanofibrous mats were experimentally determined. Firstly, mats of dimension 5 cm^2 were dried overnight at 60 °C in a hot air oven, and their dry weight was measured. The mats were then soaked in PBS solution, and the new weight was measured at intervals of 12, 24, 48, and 72 h. Filter papers were used to soak out excess water on the mat before weighing to reduce errors and exaggerated results. Concurrently, degradation analysis was conducted over 3 weeks, and the data were recorded weekly. The swelling ratio and degradation percentage were calculated using Equations 6 and 7, respectively.

$$\text{Swelling ratio} = (W_w - W_d)/W_d \text{ x } 100 \quad \text{... (6)}$$

$$\% \text{ Degradation} = (W_d - W_f)/W_d \text{ x } 100 \quad \text{... (7)}$$

View Article Online
DOI: 10.1039/D5MA01301A

Here W_w = weight of the wet sample; W_d = original dry mass of the sample; and W_f = weight of the dry sample after degradation. The test was conducted three times, with the average values representing the results

2.15 Cytotoxicity Analysis.

The cytotoxic effect of the nanofibrous mats was investigated on Vero cell lines. Vero cells were maintained in Dulbecco's Modified Eagle's Medium (DMEM) with 1% of penicillin-streptomycin (1:1), 0.2% of gentamycin, and 10% of fetal bovine serum (FBS). 12×10^4 cells per 800 µL were seeded in a 12-well plate and incubated at 37 °C with 5% CO_2. After 24 h, autoclaved samples were added to each well. Cytotoxicity was evaluated by incubating for 48 h and observed under an inverted light microscope. Each sample was analyzed using triplicate cells.

2.16 Hemocompatibility analysis

Hemocompatibility of the electrospun nanofibrous mats was evaluated through whole blood clotting and hemolysis assays. For the hemolysis assay, the method reported by Jia et al. [25] was followed. Briefly, a 9 mL working suspension of diluted blood was prepared by transferring 4 mL of freshly collected anticoagulated male rabbit blood into a 15 mL Falcon tube, followed by dilution with 5 mL of phosphate-buffered saline (PBS), maintaining a blood-to-PBS volume ratio of 4:5. The nanofibrous mats were first cut into 1.5 cm diameter discs and conditioned in PBS solution at 37 °C to attain equilibrium swelling, then transferred to a 15 mL Falcon tube and 10 mL of PBS solution was added to each tube. For the negative and positive control groups, 10 mL of PBS solution and 10 mL of pure water were added, respectively. The tubes were then placed in a water bath incubator at 37 °C for 30 minutes. To each tube, 200 µL of diluted anticoagulant rabbit blood was added, and the incubation was carried out for 1 h. After the second incubation,

View Article Online
DOI: 10.1039/D5MA01301A

the samples were centrifuged at 2500 rpm for 15 min. The absorbance of the supernatant was obtained using UV-Vis spectrophotometer at a wavelength of 540 nm to determine the concentration of released hemoglobin in the supernatant. The hemolysis ratio for each sample was quantified based on Equation 8.

The whole blood clotting properties of the nanofibers were determined by the method described in the previous studies [26]. The collected anticoagulated male rabbit blood was recalcified by adding 0.2 M CaCl solution in a 10:1 vol ratio to initiate the clotting. to obtain required anticoagulant whole blood. The preconditioned 1.5 cm diameter disc samples were slightly dried by gently placing them on a filter paper to remove excess PBS, and then transferred to a petri dish. 20 µL of recalcified blood was dropped on the nanofibrous mat surface, the control group was dropped on the bare petri dish surface. Blood was allowed to coagulate at 37 °C for 3 minutes, the sample were then transferred into a Falcon tube and the coagulation was terminated by the addition adding of 10 ml of distilled water and swirled gently without destroying the clot. Non-clotted blood underwent hemolysis to release hemoglobin into the DI water. The absorbance of the solution was determined by a spectrophotometer at 540 nm. Blood coagulation index (BCI) was calculated based on Equation 9 [26]. All procedures with animals were performed in accordance with the Institutional Ethical Guidelines for Animal Experiments of the University of Dhaka (Dhaka, Bangladesh).

$$HR\% = \frac{A_{sample} - A_{negative\ control}}{A_{positive\ control} - A_{negative\ control}} \times 100 \quad \ldots (8)$$

$$BCI\ (\%) = \frac{(I_s - I_0)}{(I_r - I_0)} \times 100\% \quad \ldots (9)$$

View Article Online
DOI: 10.1039/D5MA01301A

Where A_{sample} represents the sample absorbance, $A_{negative}$ control indicates negative control absorbance, and $A_{positive}$ control represents positive control absorbance. Whereas, where I_s was the absorbance of supernatant in sample group, I_r was the absorbance of the supernatant in the control group, and I_0 was the absorbance of deionized water. The experiments were conducted in triplicate.

2.17 *In vivo* wound healing study.

In vivo wound healing studies were conducted on male mice weighing approximately 40 g. The ethical clearance for this experiment was granted by the Faculty of Biological Sciences at the University of Dhaka (letter no 268/Biol.Scs, dt. 26-09-2024). The Swiss albino mice were maintained under standard conditions and provided with pellets and water. The mice were anaesthetized to render them unconscious for approximately 20 min using ketamine HCl USP injection (IM/IV) as per the guidelines provided by the University of Pennsylvania's International Animal Care and Use Committee (IACUC). Using a trimmer, the dorsal fur of the mice was smooth-shaved, and the estimated wound part to be formed was marked on the interscapular area at 5 mm from the ears. Next, a wound of about 1 cm in diameter and 1 mm in depth with minimal bleeding was prepared using surgical scissors and a blade. Additionally, the epidermal and dermal layers were removed to create a full-thickness wound. The as-prepared nanofibrous mats were cut into 1.5 cm^2 sizes and UV sterilized for 20 min before preconditioning for 2 min in PBS solution. Finally, the mat was gently placed on the wound site using forceps. The negative control remained untreated. Wound healing was evaluated by observing the wound morphology, contraction, and re-epithelialization with the naked eye. Furthermore, wound closure was monitored by taking digital images at 2, 7, and 14-day intervals using a Vivo Y28 phone camera equipped with a 50MP wide-angle lens at a fixed height. The wound closure rate (WCR) was calculated by measuring the wound area using the following equation 10.

View Article Online
DOI: 10.1039/D5MA01301A

$$WCR = \left(\frac{A_0 - A_t}{A_0}\right) \times 100 \quad \text{... (10)}$$

Where A_0 is the total wound area at day 0 and A_t is the total wound area at day t.

2.18 Histopathological examination.

To assess healing and inflammation in the wound areas, mice were euthanized on days 2, 7, and 14 of the *in vivo* wound healing study. Wound site tissues, including the surrounding muscle and skin, were excised and fixed in 10% buffered formalin for 24 h. Tissues were then dehydrated through a graded ethanol series (70%, 80%, 95%, and 100%, each for 2 h), cleared with xylene, embedded in paraffin, and sectioned into 4 μm-thick slices using a Leica microtome. Following deparaffinization and rehydration through a descending ethanol series (100%, 95%, 70%) and water, sections were stained with Hematoxylin & Eosin (H&E) and Masson's Trichrome (MT) according to standard protocols. Histological evaluation focused on the following parameters: necrosis, inflammatory infiltrates, hemorrhage, granulation tissue, re-epithelialization, epidermal thickness, and collagen deposition. Digital images were captured at 10× and 20× magnifications using a brightfield microscope (Zeiss Axio Scope A1, Germany). Granulation tissue areas were quantified using ImageJ software. Re-epithelialization was measured by calculating the distance between the left and right wound edges; the total re-epithelialized tissue area was defined as the sum of the new epithelium formed from both edges.

2.19 Histomorphometry analysis

For general histoarchitecture and epithelial regeneration assessment, the H and E stained tissues were analyzed. Epithelial thickness is used as an indicator of epithelial maturation in the wounded area. The epithelial thickness was measured as the distance of a new epithelial layer coverage across the wound bed using Image-J software. Before taking any quantitative measurements, the

View Article Online
DOI: 10.1039/D5MA01301A

scale was set manually for each image based on the scale bar embedded at the time of acquisition. Measurements were taken from multiple randomly selected fields per section and averaged to obtain a representative value for each sample [28]. Collagen deposition and extracellular matrix remodeling were evaluated using Masson's Trichrome staining. Collagen-positive areas (stained blue) were quantified as percentage area fraction within the wound region of interest (ROI) using standardized thresholding across all images to ensure comparability. The same image analysis workflow and threshold parameters were applied to all experimental groups and time points. This technique functions based on separating different colour channels in the stained tissue sections to isolate the collagen fibers and then quantifying them through thresholding and image analysis [29]. Angiogenesis was assessed by quantifying blood vessel density in histological sections. Vessel counts were performed manually in randomly selected high-power fields (HPF, 400× magnification). A structure was considered a blood vessel if it contained a clearly identifiable lumen lined by endothelial cells. Vessel density was expressed as the number of vessels per HPF. For each parameter, at least 5–10 non-overlapping fields per section and multiple sections per sample were analyzed to minimize sampling bias. Data were expressed as mean ± standard deviation (SD). Statistical comparisons between groups were performed using one-way or two-way ANOVA followed by appropriate post hoc tests, with $p < 0.05$ considered statistically significant

2.20 Statistical analyses.

All experiments were carried out in triplicate. The data are presented as mean ±standard deviation (SD). Statistical analysis was performed using one-way ANOVA with a significance level set at 0.05.

View Article Online
DOI: 10.1039/D5MA01301A

3.0 RESULTS AND DISCUSSION.

3.1 Synthesis and characterization of CuO, GO, and CuO-GO NC.

The nanoparticles of CuO were synthesized via a simple green synthesis method using chitosan, a polysaccharide, since chitosan can act as a reducing and capping agent. CS prevents the agglomeration of the NPs through electrostatic repulsive forces to overcome the Van der Waals forces between the individual atoms. Ideally, the molecules can self-assemble with CS acting as a capping and stabilizing agent through coordination of its amino and hydroxyl groups with CuO NPs surfaces, restricting particle growth, and yielding smaller, well-dispersed nanoparticles [18]. CS was employed as a transient reducing/capping agent and copper oxide nanoparticles were used after calcination. Chitosan was decomposed after calcination; this was evidenced by the FTIR and XRD analyses.

GO was synthesized following the modified hammer method as reported in our previous paper [30]. The conversion of bulk graphite to GO involves three steps. First, graphite is converted to the sulfuric acid-graphite intercalation compound (H_2SO_4-GIC). Second, the GIC is transformed into pristine graphite oxide (PGO). Finally, PGO reacts with water to form GO [31].

The composite of GO and CuO can lead to a productive combination of the properties of the two species compounds, which can lead to a novel series of next-generation materials with superior features. We found these hybrid materials worth exploring. A possible mechanism for the formation of GO-CuO NC is as follows: GO, with oxygen-containing functional groups on its basal planes and edges, provides anchor sites for nanoparticles formed in situ to attach. Initially, positive Cu^{2+} ions in the solvent are easily adsorbed onto the negatively charged GO sheets through electrostatic forces. Due to the rapid hydrolysis of CuO, many nuclei form quickly. The oxygen

View Article Online
DOI: 10.1039/D5MA01301A

atoms in these growing crystal units then bond with the functional groups on the GO sheets through intermolecular hydrogen bonds or coordination bonds, facilitating further crystallite growth [32].

The as-prepared CuO, GO, and CuO-GO NC were characterized with ATR-FTIR, XRD, SEM and TEM analyses.

ATR-FTIR spectroscopy of CuO-GO NC.

The FTIR spectra of GO, CuO, and CuO-GO NC are presented in **Figure 1a** to investigate the interaction and functional group modifications upon composite formation. The ATR-FTIR spectrum of GO (**Figure 1a**), displays a broad absorption band centered at 3400 cm^{-1}, which corresponds to the O-H stretching vibration, indicative of hydroxyl functional groups. A distinct peak at 1726 cm^{-1} is attributed to the C=O stretching vibration of the carboxylic groups. The strong peak at 1615 cm^{-1} is associated with bending of H-O-H from absorbed water. The band at 1371 cm^{-1} originates from the C-OH deformation, while the peak at 1224 cm^{-1} can be assigned to the C-O-C asymmetric stretching of epoxy groups. Additionally, the absorption band at 1059 cm^{-1} is linked to the C-O stretching of alkoxy groups [33]. The FTIR spectra of chitosan–CuO NCs and calcined CuO NPs are shown in **Figure S1**. The spectrum of the chitosan–CuO shows a broadened O–H/N–H stretching band at 3340 cm^{-1}. Changes in the N–H bending peak at 1535 cm^{-1} indicate Cu^{2+} ions primarily coordinate with chitosan amino groups. In contrast, calcined CuO NPs exhibit the disappearance of organic-related bands, retaining only weak surface hydroxyl features and the characteristic Cu–O lattice vibration at 455 cm^{-1} and confirming the formation of a pure monoclinic CuO phase.

The ATR-FTIR spectrum of the GO-CuO NC (**Figure 1a**) divulges the presence of key functional groups associated with both GO and CuO NPs. Distinct absorption bands observed at 581 and 480

View Article Online
DOI: 10.1039/D5MA01301A

cm^{-1} correspond to the stretching vibrations of the Cu-O bond, confirming the successful incorporation of CuO nanoparticles onto the GO nanosheets. Additionally, characteristic peaks located at approximately 3450, 1620, 1370, and 1070 cm^{-1} can be assigned to O-H, and C-OH, and C-O functional groups of GO, respectively. These observations indicate that the oxygen-containing functionalities of GO were preserved even after the formation of the composite with CuO [34]. The observed spectral shifts and merging of absorption bands suggest weak interactions between CuO nanoparticles and oxygenated functional groups on GO, potentially via electrostatic force or hydrogen bonding. These interactions may enhance the dispersion stability and interfacial compatibility within the composite system.

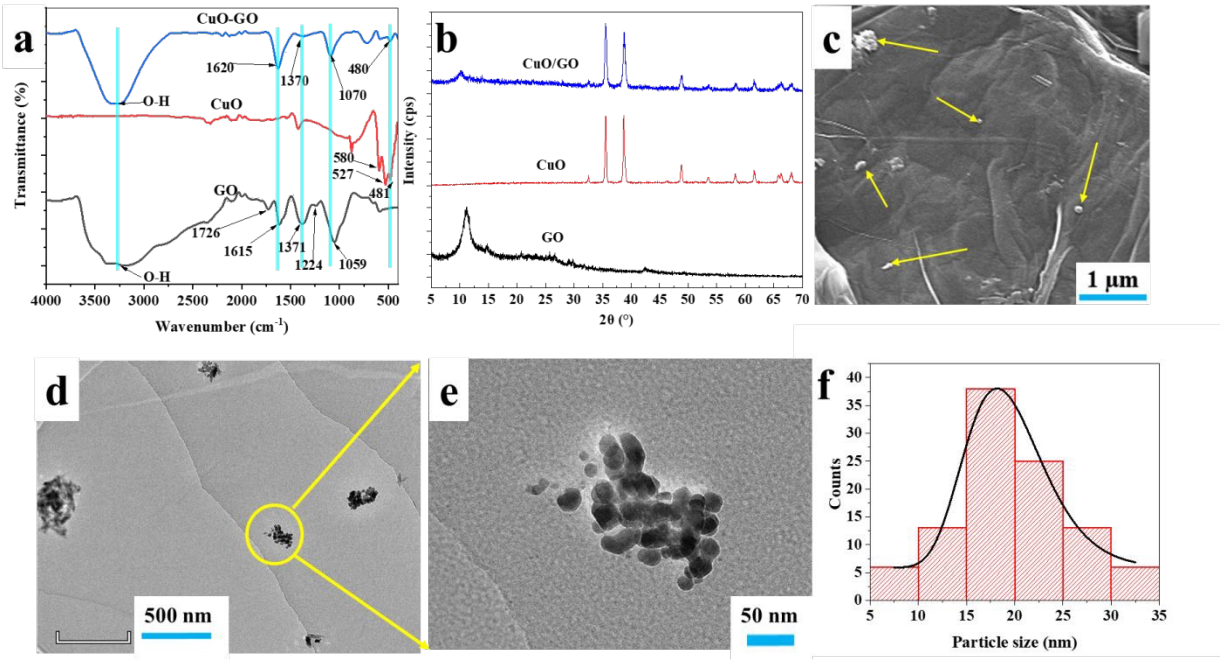

Figure 1. Comprehensive characterization of the CuO–GO NCs: (a) ATR-FTIR spectra and (b) XRD patterns elucidate the chemical structure and crystallinity, (c) the SEM image highlights CuO nanoparticles (yellow arrows) uniformly decorated on the GO surface; (d) Low and (e) high-

View Article Online
DOI: 10.1039/D5MA01301A

resolution TEM images further confirm nanoparticle dispersion and interfacial integration, and (f) CuO nanoparticle size distribution plot.

X-Ray diffraction analysis.

Figure 1b shows the XRD spectra for CuO, GO, and CuO-GO NC. To identify the crystal phase of CuO, the sample was thermally treated in a muffle furnace at 600 °C for 4 h to decompose the organic components. This temperature was sufficient to completely remove chitosan, resulting in a pure crystalline CuO phase. XRD analysis reveals a single monoclinic phase. Diffraction peaks at 32.51, 35.44, 38.48, 48.80, 53.46, 58.1, 61.36, 65.81, and 68.04° are assigned to the (110), (-111), (111), (-202), (020), (202), (-113), (311), and (220) respectively, diffraction planes of monoclinic CuO which agree well with the standard JCPDS card no. 00-044-0706 [35] Previously, similar results were reported elsewhere [36].

The XRD spectrum of GO has a dominant diffraction peak at 2θ value of 9.80°corresponding to the (002) diffraction plane of GO [37]. A very low-intensity diffraction peak of reduced GO at around 26.81° was also observed. The interlayer spacing (0.87 nm) is found to be larger than that of pristine graphite (0.34 nm), which can be ascribed to the introduction of oxygen-containing functional groups on the graphite sheets. The interlayer spacing was increased through the addition of functional groups, including C-O, C-OOH, and C-OH, leading to a higher value of GO basal spacing. The broad diffraction peak at 10.07° in the CuO-GO XRD pattern is apparently due to the (002) planes of the hexagonal GO structure. The peaks at 35.30, 38.54, 48.66, 53.32, 58.38, and 61.62° correspond to the (-111), (111), (-202), (020), (202), and (-113) diffraction planes of monoclinic crystalline CuO in the CuO-GO composite [37]. It was noted that the CuO phase dominated the GO phase.

View Article Online
DOI: 10.1039/D5MA01301A

SEM analysis of the CuO-GO NC

The high-resolution SEM images (X20000) of the ultra-sonicated CuO-GO NC are depicted in **Figure 1c**, revealing underlying flake-like structures that resemble those of the bare GO (**Figure S2**). At the same time, this surface is covered with additional CuO nanoparticles that contrast differently with the underlying GO sheet. From this image, it was vividly possible to distinguish CuO NPs from the GO nanosheet. The CuO NPs appeared spherical and randomly decorated on the GO surface. The small-sized NPs are attributed to the ultrasonication method employed during synthesis. The high pressure during sonication increases the fluid temperature by cavitation, inducing high local shear, dispersing the particles, and breaking them into smaller sizes [38].

Furthermore, the low magnification (X7000) SEM image (**Figure S2**) revealed that the GO sheets had folds and formed wrinkled flakes. Studies have shown that the structure of GO is affected by intrinsic and extrinsic parameters, such as thermal fluctuation, defects, functionalization, and applied stresses [39]. Functional groups and structural defects present on the basal planes of GO can change the electronic structure of carbon atoms from sp2 to sp3 hybridization, thereby deviating carbon atoms from the original plane, resulting in atomic-level wrinkling [39]. Another possible explanation for the wrinkles might be a result of GO-water interactions. During water-casting, GO sheets crumble due to drying stresses associated with surface tension as water evaporates. Moreover, the CuO nanoparticles were non-uniformly distributed. Probably, the oxygen-containing functional groups (hydroxyl, carboxylic, and epoxy) on the GO surface prevent the aggregation of metal oxide species.

TEM analysis

View Article Online
DOI: 10.1039/D5MA01301A

The TEM analysis was also performed for the GO sheets, CuO NPs, and the CuO-embedded GO nanocomposite to analyze the size and shape of the NPs and the nanocomposite. Low magnification TEM images of the CuO-GO NC are depicted in **Figure 1d**, which further confirmed that the CuO NPs were widely spread and uniformly embedded on the surface of the GO sheets. From the high-magnification TEM image in **Figure 1e**, it was observed that the CuO nanoparticles were spherical, with a size range of 5-35 nm and an average size of 19 nm, which was determined by measuring 100 particles picked randomly and plotting the data in a size distribution histogram shown in **Figure 1f**.

Furthermore, the TEM image of GO sheets in **Figure S3** shows a thin, flake-like GO sheet with its edges slightly scrolled and folded backward. This folding behavior is characteristic of graphene oxide (GO), which possesses various oxygen-containing functional groups on its surface. These functional groups not only increase the hydrophilicity of the sheets but also prevent restacking and regraphitization. The tendency of GO sheets to fold upon drying helps preserve their high surface area.

3.2 Viscosity and electrical conductivity of spin solutions.

The viscosity and conductivity of the electrospinning solution directly impact the nanofibrous mat properties, such as fiber diameter and morphology. Therefore, each solution was analyzed before electrospinning by measuring viscosity and electrical conductivity (**Figure 2)**. Sequential flow curve measurements were conducted to evaluate the influence of varying shear rates and incremental CuO-GO concentrations on the viscosity under ambient conditions.

As illustrated in **Figure 2a**, the viscosity versus shear rate profile demonstrates that all formulations exhibited a pronounced decrease in viscosity with increasing shear rate (3-25 s^{-1}),

View Article Online
DOI: 10.1039/D5MA01301A

indicative of shear-thinning behavior. This non-Newtonian pseudo plastic behavior was consistently observed in both the pristine PVA/CS solution and the CuO-GO nanocomposite-loaded PVA/CS polymer solutions loaded with 0.75% to 2% (w/w) of CuO-GO NC.

Furthermore, at a constant shear rate of 3 s^{-1}, an incremental increase in CuO-GO nanocomposite content within the PVA/CS polymer solutions led to a progressive reduction in shear viscosity. Specifically, the viscosity decreased from 0.73 Pa·s in the unmodified PVA/CS solution to 0.70, 0.66, 0.61, and 0.59 Pa·s upon incorporation of 0.75%, 1.0%, 1.5%, and 2.0% (w/w) CuO-GO, respectively as seen in **Table 1**. However, the observed increase in viscosity upon incorporation of CS into the PVA solution can be attributed to enhanced molecular interactions, including both intramolecular and intermolecular hydrogen bonding, as well as electrostatic interactions between the PVA and CS chains. Such interactions facilitate polymer chain entanglement and trigger conformational rearrangements, leading to enhanced flow resistance [56].

Additionally, electrostatic repulsion among the positively charged CS chains contributes to polymer chain extension and expansion of the overall network structure, further elevating viscosity. It is well-established that polymer concentration and molecular weight significantly influence solution viscosity [40]. In this study, a 10% (w/v) of high molecular weight PVA and 2% (w/v) of CS with a low molecular weight and 90% degree of deacetylation (DA) were utilized, which likely intensified these effects. Conversely, increasing the CuO-GO nanocomposite content within the PVA/CS matrix resulted in a gradual reduction in viscosity. This reduction can be attributed to a decrease in polymer chain entanglement density, likely arising from nanofiller-induced structural disruption. A study by Weir et al. [41] demonstrated that in polymer-GO NC, the high aspect ratio and strong interfacial confinement effects of GO distort polymer chain conformations, thereby diminishing the number of interchain entanglements, as evidenced through

View Article Online
DOI: 10.1039/D5MA01301A

bulk rheological measurements. Remarkably, their findings revealed that as little as 0.5% of GO (by volume) was sufficient to significantly reduce the average chain dimensions in the bulk nanofibrous matrix, supporting the observed viscosity-lowering effect in our system.

Regarding the electrical conductivity of the electrospinning solutions, the pure PVA solution has a conductivity of 0.06 mS/cm. The PVA/CS composite solution had a conductivity of 0.25 mS/cm. The addition of 0.75% CuO-GO composite to the PVA/CS solution resulted in an increase in conductivity to 0.88 mS/cm. However, a further increase in the concentration of CuO-GO to 1%, 1.5%, and 2% in the PVA/CS solution resulted in an increasing conductivity to 1.09, 1.23, and 1.48 mS/cm, respectively, as seen in **Figure 2b**.

PVA is a water-soluble, semicrystalline polymer that forms long-range hydrogen bonds in aqueous solution. It is generally considered an insulator due to its poor electrical conductivity [42], on the other hand, CS is an amino polysaccharide molecule with a strong positive charge [43]. Adding CS to the acetic acid solution of 10 (w/w)% PVA increases the solution's conductivity and viscosity. This is because at low pH below 6.5, using acetic acid, the amino groups (NH_2) of CS were protonated (NH_3^+), thereby giving a positive charge to the polymer backbone.

It has been reported that the conductivity of CS solution is a result of the protonation of NH_3^+ groups that leads to mobile OH^- ions that can move freely and give rise to an ionic current[44]. Additionally, the proton (H^+) is dissociated from acetic acid and results in a free amino group in the chitosan backbone when protonated ($-NH_2 + HAc \leftrightarrow -NH_3^+ + Ac^-$). While the water molecules absorbed in the chitosan chains can form hydrogen-bond sites for the proton transferring from amino groups to water molecules ($-NH_3^+ + H_2O \leftrightarrow -NH_2 + H_3O^+$) .

View Article Online
DOI: 10.1039/D5MA01301A

It was also noted that adding 0.75wt%, 1wt%, 1.5wt%, and 2wt% CuO-GO NC into the PVA/CS composite solution resulted in a 252%, 336%, 392%, and 492% increase in the conductivity, respectively. The integration of CuO-GO NC into the PVA/CS nanofibrous matrix significantly enhanced the electrical conductivity of the polymer solution. This enhancement is attributed to the synergistic interaction between GO's extended π-conjugated network and the semiconducting nature of CuO, which likely facilitated the formation of interconnected conductive pathways within the polymer nanofibrous matrix [45].

The conductivity of polymer solutions impacts the Taylor cone formation. The applied voltage induces an electric field that causes charge buildup on the polymer surface. When it exceeds the polymer's surface tension, a jet of polymer is drawn towards the collector. Increased conductivity of the polymer solution enhances charge buildup, resulting in a more distinct Taylor cone with improved jet stability (stretch and elongation of jet), ultimately producing thin fibers [60].

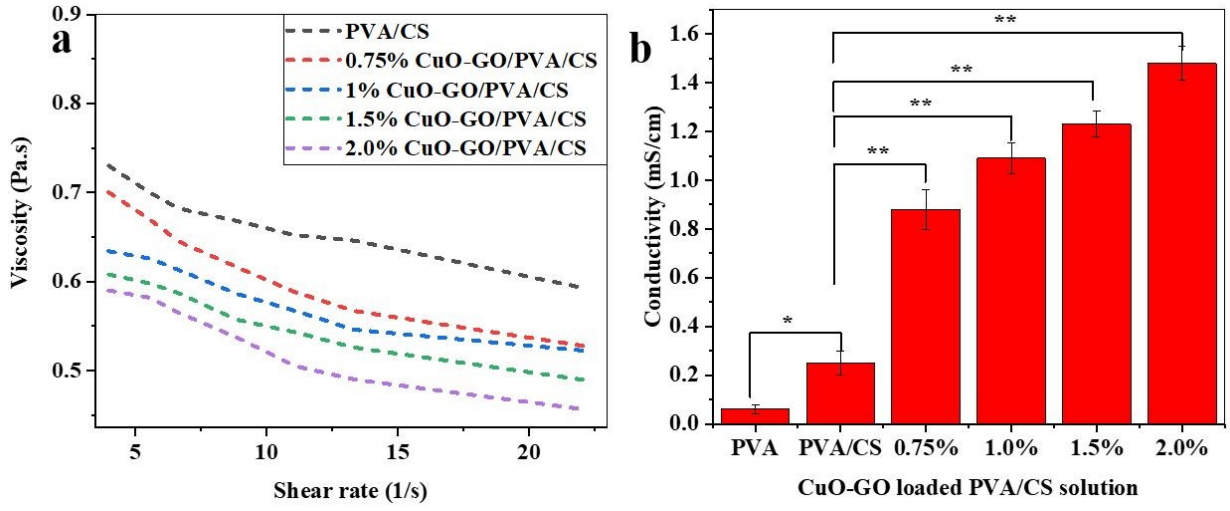

Figure 2. (a) Effect of CuO–GO nanocomposite (NC) incorporation on the rheological and electrical behavior of the PVA/CS polymer solution: (a) shear viscosity versus shear rate and (b) solution conductivity, shown for the neat polymer system and after the addition of 0.75, 1.0, 1.5,

View Article Online
DOI: 10.1039/D5MA01301A

and 2.0 wt% CuO–GO NC. Data are shown as mean ± SD (n = 3). Statistically significant differences were considered for *p ≤ 0.05, **p ≤ 0.01

3.3 ATR-FTIR analysis of nanofibers.

The distinctive molecular structures of PVA, CS, and PVA/CS nanofibers were identified from the ATR-FTIR spectra (**Figure 3)**. The spectra of pure PVA, CS, un-crosslinked PVA/CS, and crosslinked PVA/CS nanofibrous mat are depicted in **Figure 3a**. IR spectrum of PVA shows broad peaks at 3288 cm^{-1} associated with the O-H stretching vibration from the intra- and intermolecular hydrogen bonds and peaks at 2940 and 2911 cm^{-1} related to the asymmetric and symmetric C-H stretching vibrations of $-CH_2$, respectively. The characteristic bands detected at 1714 cm^{-1} indicate the C=O bonds' stretching vibrations associated with the acetyl group of the polyvinyl acetate [47]. The peak at 1418 cm^{-1} indicates the scissoring $-CH_2$ group. Additionally, a peak at 1138 cm^{-1} corresponds to the stretching of the C-O bonds associated with the crystalline portion of PVA. The characteristic peaks at 916 and 840 cm^{-1} indicate the presence of skeletal vibrations in PVA [49].

Pure CS spectra have a broad band between 3650 to 2980 cm^{-1} due to the O-H and N-H stretching vibrations. The peaks at 2916 and 2870 are attributed to the C-H stretching vibrations. The band associated with the asymmetric stretching vibration of the C=O; is noted at 1652 cm^{-1}, while that at 1581 cm^{-1} is assigned to the N-H bending vibration. The bands at 1418 cm^{-1} is attributed to the asymmetric C-H bending vibration [49]. Further, the bands at 1066 cm^{-1} is assigned to the C-O-C stretching vibration of the glycosidic bond that forms the chitosan chain [10].

The IR spectra of PVA/CS nanofibrous mats exhibit characteristic peaks from the PVA and chitosan precursors. The peak at 3316 cm^{-1} correspond to overlapping O-H, N-H vibrations whereas the peak at 2925 cm^{-1} is for C-H stretching vibrations in both CS and PVA [50]. The shift

View Article Online
DOI: 10.1039/D5MA01301A

of the C-H stretching peak from 2870 cm^{-1} in pure chitosan to 2909 cm^{-1} in the PVA-CS composite indicates enhanced molecular interactions. This shift is attributed to hydrogen bonding between PVA and CS. The ionization of the major amino groups in chitosan is evidenced by the peaks at 1590 cm^{-1} associated with the symmetric deformation of $-NH_3^+$ groups. In acidic conditions, the amine groups ($-NH_2$) in chitosan protonate to $-NH_3^+$.

Upon adding PVA, the abundant OH groups in PVA form strong hydrogen bonds with $-NH_3^+$, reducing electrostatic repulsion and altering vibrational energy. This weakens the NH_3^+ bond strength, stabilizes the chitosan structure, and shifts the peak to a lower wavenumber 1560 cm^{-1}. Additionally, the absorption peak at 1260 cm^{-1} assigned to the O-H band in PVA disappeared for PVA/CS nanofibrous mat. The crystalline-sensitive bands of chitosan at 1060 cm^{-1} and 659 cm^{-1} disappeared in PVA/CS nanofiber, thus confirming the blended nature of the PVA and CS and PVA/CS composite.

The spectra of the heat-treated PVA/CS nanofibers at 120 °C for 80 min exhibited peaks like those of PVA and CS. The O-H and N-H bands around 3630-2980 cm^{-1} appeared much narrower and sharper due to the dehydration process in the thermally treated fiber nanofibrous mats. Moreover, the identity peak linked to the crystalline part of the PVA at 1141 cm^{-1} observed in the PVA spectrum overlapped the peak at 1090 cm^{-1} for all the fiber nanofibrous mat samples [20]. After being thermally treated, this peak became much pronounced and sharper. Thus, the improvement in the mechanical properties could also be associated with the physical crosslinking effect, due to the removal of acetic acid and water residues from the microstructure of the electrospun fibers. Thermal crosslinking of PVA occurs through the loss of inter- and intramolecular water, leading to enhanced crystallization. As water molecules evaporate, hydrogen bonds between PVA and

View Article Online
DOI: 10.1039/D5MA01301A

water break, allowing PVA chains to pack more closely and form stronger interchain hydrogen bonds [49].

This increased crystallinity improves the nanofibrous material's mechanical strength, thermal stability, and reduces water solubility. When blended with chitosan, thermal crosslinking further strengthens hydrogen bonding between the two polymers, modifying the composite's structural and functional properties. This explains why the heat-treated PVA/CS nanofibers showed less degradation in PBS over the study period of 3 weeks (Figure 7).

Similarly, the molecular interaction between the CuO-GO NC and the PVA/CS nanofiber was studied by ATR-FTIR analysis. **Figure 3b** shows the respective spectra of the PVA/CS nanofiber loaded with different wt% of CuO-GO NCs and the magnified portion, highlighting the key peaks that can be used to confirm the interaction between the CuO-GO NC and PVA/CS nanofibers. All the nanofibrous mats were thermally crosslinked. The weight ratio of CS: PVA (1:10), and the weight ratio of GO: CuO (1:1) were constant. However, the loaded percentage of the CuO-GO NC into the PVA/CS polymer blend solution varied between 0.75%, 1%, 1.5%, and 2%. The characteristic epoxy peak at 1224 cm^{-1} in GO is capable of reacting with the primary amine ($-NH_2$) groups of CS, resulting in the formation of secondary amine (C-NH) linkages [51]. However, due to the proximity of the IR absorption bands of primary and secondary amine groups, no distinct spectral shift was observed between the two, making differentiation difficult. Additionally, the carboxyl groups present on GO can also form amide bonds with amino groups on CS, but the corresponding FTIR signals for the resulting secondary amines were similarly indistinct, indicating overlapping or weak intensity in the region.

In **Figure 3c**, It is evident that the peak emerged at 1640 cm^{-1} in the CuO-GO/PVA/CS spectrum compared to GO, which is related to the N-H stretching vibration of NH_3^+ due to the transformation

View Article Online
DOI: 10.1039/D5MA01301A

of amine groups under extremely acidic synthesis conditions [52]. A noticeable shift of the amide II band from 1552 cm^{-1} to 1562 cm^{-1} was observed. This shift is attributed to the interaction between the amino groups of chitosan and the oxygen-containing functional groups of GO, particularly carboxyl and epoxy moieties [53].

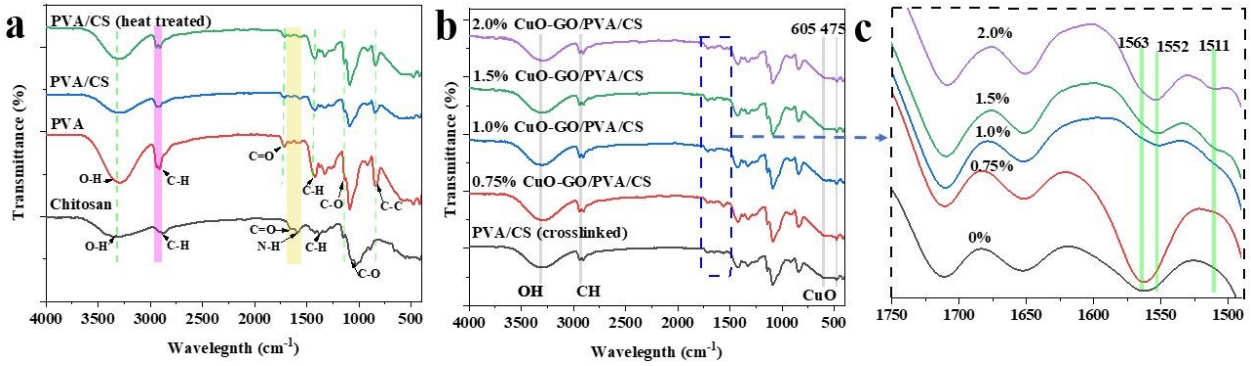

Figure 3. ATR-FTIR spectra of (a) CS, PVA, uncross-linked PVA/CS, and cross-linked PVA/CS nanofibers; (b) CuO-GO embedded PVA/CS nanofibrous mat; and (c) an expanded view of the 1500-1750 cm^{-1} region for the CuO-GO/PVA/CS nanofibrous mat.

3.4 Differential Scanning Calorimetry analysis

DSC analyses were carried out to investigate the thermal property and phase transitions of the electrospun nanofibrous mats following thermal crosslinking. In polymeric systems, glass transition temperature and melting point are critical thermal phenomena influenced by processing conditions and the incorporation of additives.

Figure 4 presents the DSC thermograms of pristine PVA/CS and CuO-GO-loaded PVA/CS nanofibrous mats, with CuO-GO contents ranging from 0.75 wt% to 2.0 wt%. A broad endothermic peak centered around 50 °C was observed in all samples, attributed to the evaporation of tightly bound water, which is involved in H-bonding interactions with the hydroxyl and amino

View Article Online
DOI: 10.1039/D5MA01301A

groups of CS and the hydroxyl groups of PVA [54]. Upon removal of bound water, the PVA/CS nanofibrous mat displayed a glass transition temperature (T_g) at approximately 78 °C. A slight downward shift in T_g was recorded with increasing CuO-GO content, indicating changes in chain mobility. A distinct endothermic peak at 214 °C was observed, corresponding to the crystalline melting temperature (T_m) of PVA [54]. This melting peak systematically shifted to lower temperatures of 208, 206, 205, and 204 °C for the nanofibers containing 0.75%, 1.0%, 1.5%, and 2.0 wt% of CuO-GO, respectively. No melting peak for chitosan was detected, as chitosan is not thermoplastic; instead, it undergoes degradation before melting due to its strong intermolecular hydrogen bonding.

The decrease in T_m with increasing CuO-GO content is attributed to the interaction and dispersion of CuO-GO within the polymer matrix. At lower concentrations, CuO-GO may act as nucleating agents that promote crystallization. However, at higher loadings, particle agglomeration likely occurs, disrupting the hydrogen bonding network and inhibiting crystal growth, thereby reducing T_m and overall crystallinity [55]. The latent heat of melting (ΔH_m) values were found to be 41.07, 32.66, 19.54, 16.00, and 12.74 J/g for the pure PVA/CS nanofibrous mat and the mats loaded with 0.75 wt%, 1.0 wt%, 1.5 wt%, and 2.0 wt% CuO-GO, respectively. Furthermore, Using a reference value of ΔH_m = 138.6 J/g for 100% crystalline PVA [56], the degree of crystallinity (Xc) of the nanofibers was calculated. Overall, the incorporation of CuO-GO NCs led to a notable reduction in crystallinity (**Figure S4**). This decline can be attributed to the disruption of the crystalline structure of PVA during the electrospinning process, which involves rapid solidification and high elongation forces. Additionally, the use of solvents during the preparation phase, high elongation rate, and the rapid solidification process during the electrospinning may have further impaired the development of the crystalline domain [49]. The relatively high thermal stability of the developed

View Article Online
DOI: 10.1039/D5MA01301A

nanofibrous mats suggests their suitability for applications such as wound dressing, where resistance to autoclave sterilization and thermal crosslinking is essential. Interestingly, the decrease in crystallinity and melting point also implies increased porosity and surface area, both advantageous properties for biomedical applications. The presence of PVA contributes to enhanced thermal stability across all formulations [56].

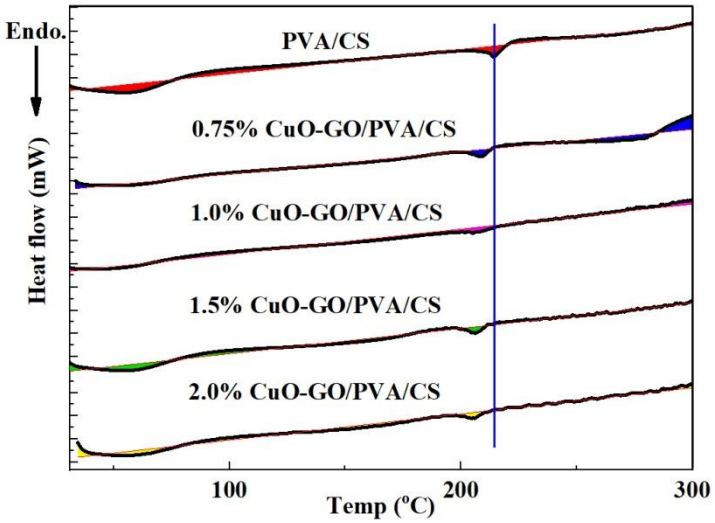

Figure 4. DSC spectra of PVA/CS and different wt% of CuO-GO embedded PVA/CS nanofibrous mats

3.5 SEM analysis of nanofibrous mats.

Nanofiber morphology has a significant impact on the behavior of wound dressing materials in medicinal applications. It has a direct influence on cell culture and drug release properties. Various factors, including the properties of the electrospin solution, electrospinning parameters, and environmental conditions, affect the nanofiber morphology. Designing a nanofiber with uniformly distributed morphology (including fiber orientation, diameter, pore size, and density) is a delicate art of engineering design. Here, we designed PVA/CS nanofibers mat by varying the CuO-GO concentration while keeping all other factors constant.

View Article Online
DOI: 10.1039/D5MA01301A

The SEM images and size distribution histograms of the as prepared nanofibrous mats are displayed in **Figure 5**. The average fiber size of the mats was found by measuring the diameter of 100 fibers randomly selected across the mat surface using Image J software version 1.53t. The nanofiber mat of the prepared polymer solution formulation has a random distribution with no dominant fiber orientation. The fiber randomness is likely due to the whipping motion of the spinning jet. Although it has been reported that aligned nanofibers provide good contact guidance for cell proliferation, facilitate cell-cell interactions, and promote cell alignment when compared to random fibers [57].

As shown in **Figures 5a** and **5a1**, low and high magnification, respectively. PVA/CS electrospun mats produced nanofibers with a smooth surface. In addition, the process yielded no significant droplet residues. The nanofiber diameter was 290 nm as seen in the size distribution histogram in **Figure 5a2**.

PVA has been utilized as an adjuvant to assist in spinning bead-free nanofibers of CS. The interaction between the NH_3^+ of CS and the -OH groups of PVA enhances the viscosity of the spinning solution. Furthermore, the positively charged groups of CS improve the electrical conductivity of the solution. High molecular weight PVA was used to produce a nanofibrous mat from 10% (w/v) solutions of PVA and 1wt% of CS solution by the electrospinning process. The high viscosity of the electrospun solution is due to PVA and CS chain entanglement resulted in a dense solution which contributed to the formation of thicker nanofibers.

Figure 5b and **5 b1** depict the low and high magnification images of the 0.75wt% of CuO-GO embedded PVA/CS nanofibrous mat. By adding 0.75wt% of CuO-GO into the PVA/CS polymer solution to prepare the nanofibrous mat, a decrease of 18% in average fiber diameter to 238 nm was noted, as depicted in the histogram in **Figure 5b2**. Similarly, in **Figure 5c** and **5c1**(low and

View Article Online
DOI: 10.1039/D5MA01301A

high magnification, respectively), a further increase in the concentration of CuO-GO to 1% resulted in beadles and thin nanofibers marked by a decrease in average fiber diameter to 219 nm as shown in **Figure 5c2**. Interestingly, in **Figure S5,** it was clear that the incorporation of CuO-GO enhances the nanofiber porosity, as pores of random sizes were visible from the cropped SEM images of the fiber sections shown in Figure 5c1.

Notably, **Figure 5d** and **5d1** show the SEM images of 1.5 wt% of CuO-GO loaded PVA/CS nanofibers. The mat had randomly aligned nanofibers, with a smooth surface and a average size distribution of 168 nm, as shown in **Figure 5d2**. Finally, adding 2 wt% of CuO-GO in PVA/CS polymer solution produced fibers with spindles as seen in **Figure 5e** and **5e1** (low and high magnification, respectively). The spindles are probably due to the higher concentration of CuO-GO. Furthermore, the progressive fiber thinning was evident in this sample too with a fiber mean size of 116 nm (**Figure 5d2**).

This indicates that the addition of CuO-GO to the PVA/CS polymer solution led to fiber size reduction due to an increase in charge density of the composite, prompted by the semiconductor property of CuO and the charge transfer property of GO in CuO-GO NC. High conductivity resulted in polymer jet splitting into thinner fibers, which ultimately leads to fibers of smaller diameter. Beaded fibers are associated with the instability of the polymer jets, which is in turn influenced by the balance between the viscosity and surface tension of the spin solution. The hydrogen bonds between PVA, CS, and GO played a crucial role in stabilizing the polymer jet during the spinning process.

For most cases examined here, the nanofibers' diameter decreased with the increase in CuO-GO concentration. Therefore, it can be assumed that the solution thinning, as was seen in the viscosity analysis, with increasing electrical conductivity, will lead to a small size nanofiber diameter. These

View Article Online
DOI: 10.1039/D5MA01301A

are the relevant variable parameters to compare with the fiber size. The CuO-GO NCs were not clearly distinguishable in the SEM images of the nanofibrous mats, likely due to their small size and relatively low concentration within the fiber matrix. Therefore, transmission electron microscopy was employed to confirm the presence and distribution of CuO-GO within the nanofibrous mats.

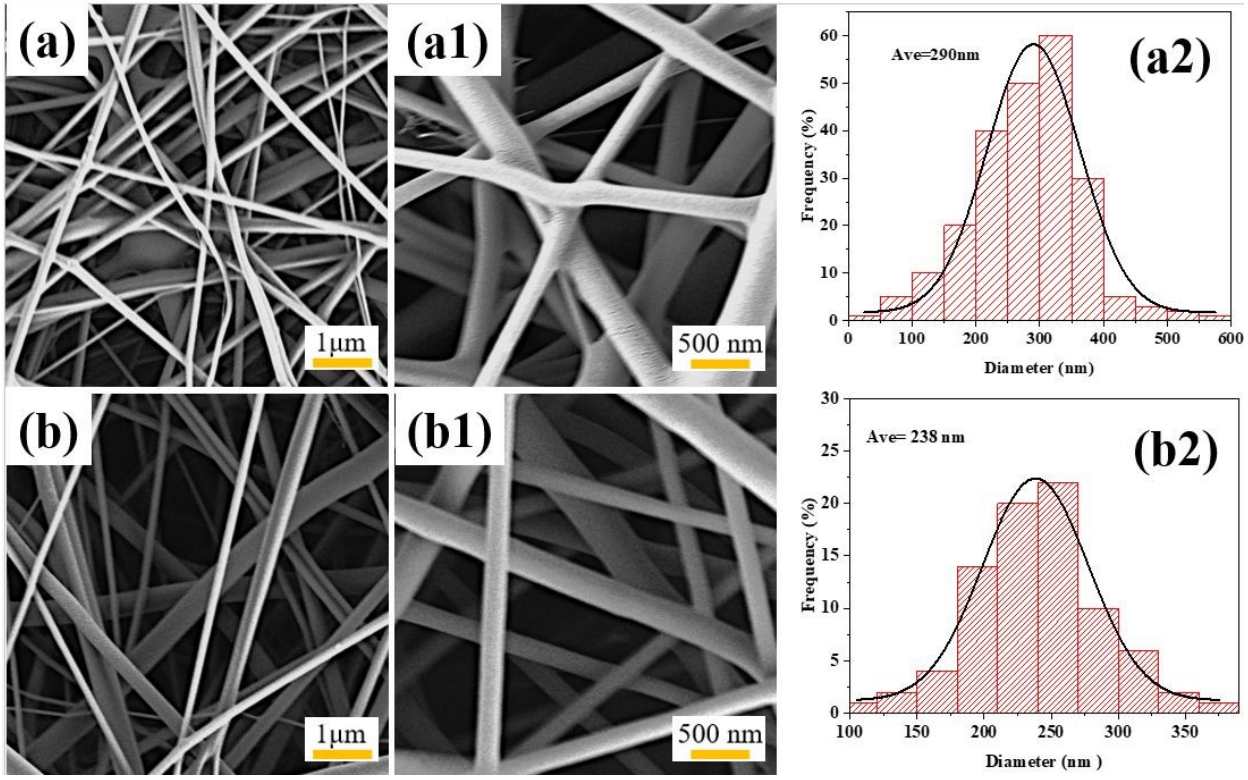

View Article Online
DOI: 10.1039/D5MA01301A

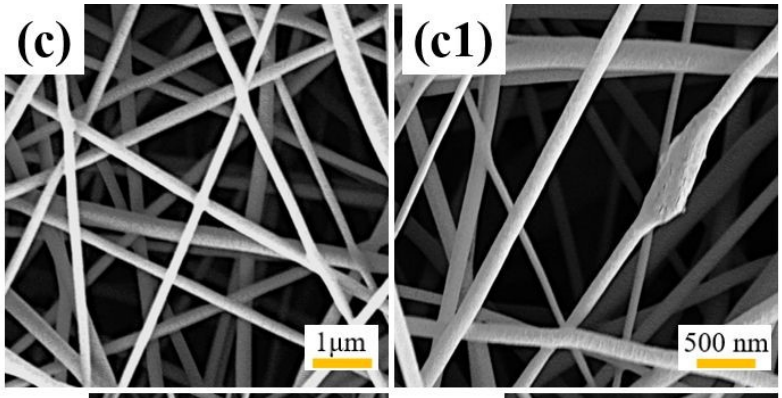

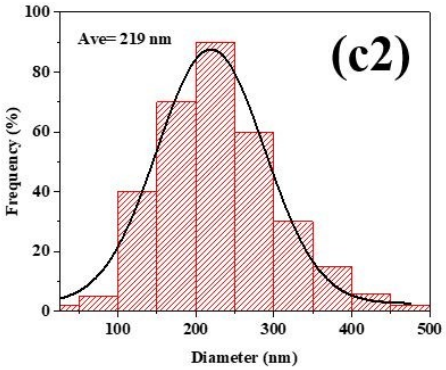

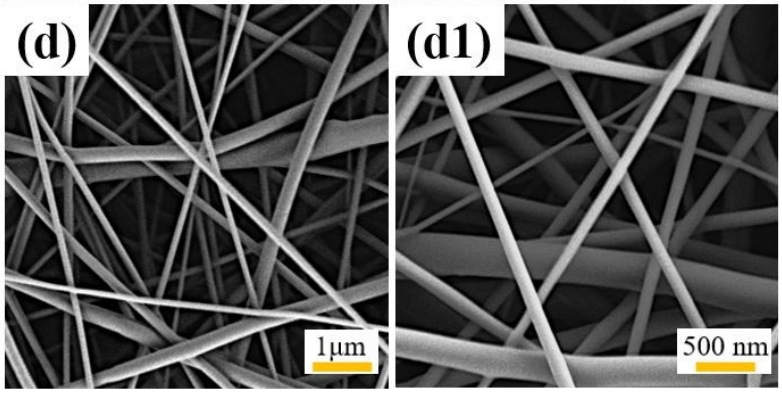

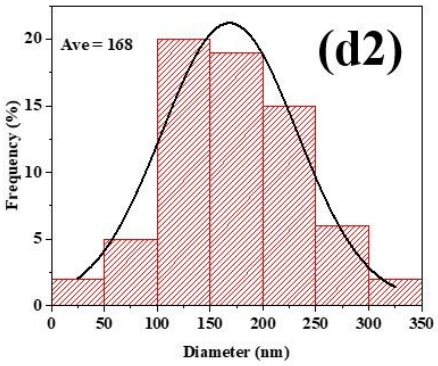

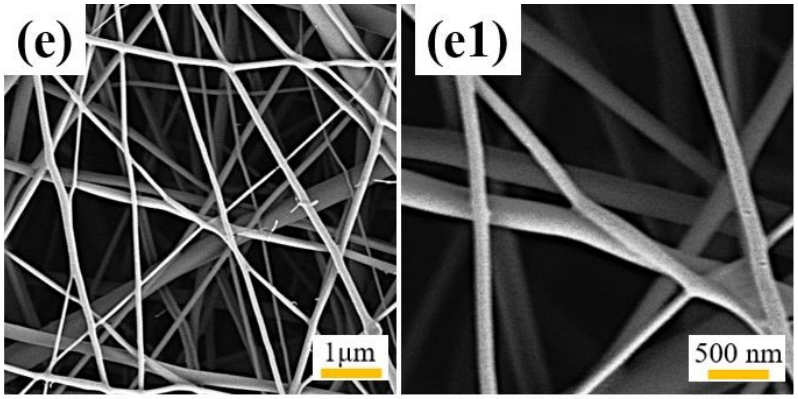

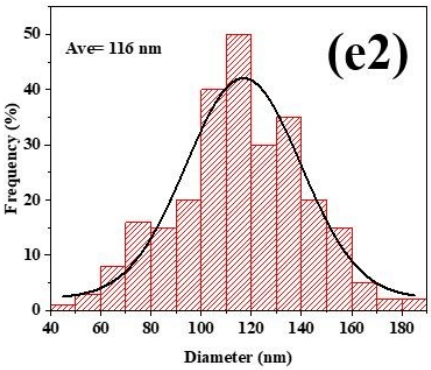

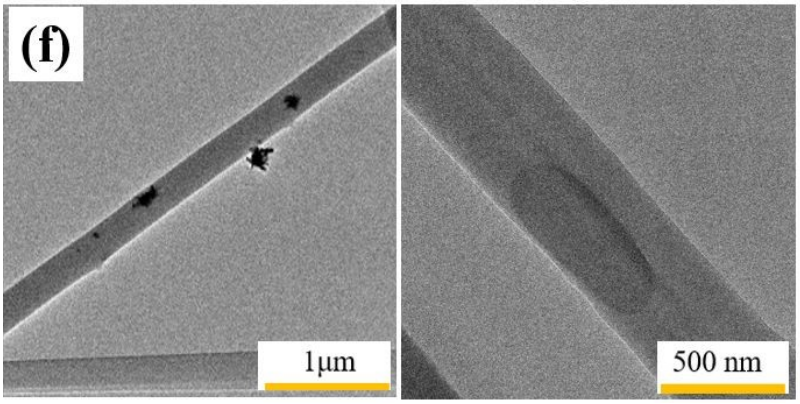

View Article Online
DOI: 10.1039/D5MA01301A

Figure 5. SEM analysis of cross-linked PVA/CS nanofibrous mats embedded with different wt% of CuO-GO nanocomposites. (a-e) FESEM images at 10,000× magnification with 0, 0.75, 1.0, 1.5, and 2.0wt% CuO-GO, respectively. (a1-e1) Corresponding high-magnification images at 40,000×. (a2-e2) Nanofiber diameter distributions for each composition. (f and f2) low and high magnification TEM images of the 1.5 wt% CuO-GO embedded PVA/CS nanofibrous mats.

Additionally, EDX analysis was employed to evaluate the elemental composition of the CuO-GO incorporated PVA/CS nanofibers. The corresponding EDX spectra of 2 wt% of CuO-GO embedded PVA/CS nanofibers are shown in **Figure S6**. As is seen, C, N, O, and Cu are the main components, which distinctly indicate that the CuO-GO was loaded inside the PVA/CS nanofiber. The elemental compositions of C, N, O, and Cu in 2 wt% of CuO-GO embedded PVA/CS were 67.54 wt%, 1.51 wt%, 29.55 wt% and 1.4 wt%, respectively as seen in **Figure S6** inset.

3.6 TEM analysis of nanofibrous mats.

High-resolution transmission electron microscopy images of CuO-GO embedded PVA/CS nanofibrous mat are depicted in **Figure 5f.** The nanofibers exhibit an elongated cylindrical shape with relatively smooth surfaces, suggesting a controlled electrospinning process. **Figure 5f** shows the dark contrast regions, indicating that localized CuO-GONC are uniformly distributed within the nanofibers. This confirms successful incorporation of CuO-GO within the PVA/CS nanofibrous structure, likely through hydrogen bonding or covalent interactions. The homogeneous dispersion of CuO-GO suggests effective interaction with the polymer nanofibrous matrix, whereas partial clustering of CuO-GO may result from aggregation during the electrospinning process. The lighter fiber regions indicate polymer-dominant areas, while the darker areas represent higher atomic density due to CuO-GO presence [58] The uniform nanofiber morphology suggests good electrospinnability and mechanical stability, while the embedded CuO-

View Article Online
DOI: 10.1039/D5MA01301A

GO nanoparticles enhance potential applications in rapid wound dressings. Overall, the TEM analysis confirms effective integration of CuO-GO into the CS/PVA nanofibrous mat, with mostly uniform distribution.

Next, XRD analysis of the nanofibrous mats was conducted to determine the effect of the CuO-GO NCs and thermal crosslinking on the crystallinity of the mats.

3.7 XRD analysis of representative nanofibrous mats

The XRD profiles of the PVA/CS and 2 wt% of CuO-GO embedded PVA/CS electrospun nanofibrous mats before and after thermal crosslinking are shown in **Figure S7.** The XRD spectra of all the samples were dominated by the PVA fraction, showing a sharp peak at 19.55°, correspond with the (101) reflection planes, respectively. A similar finding was reported by Kusjuriansah et al, [59] The characteristic diffraction peaks at 9.40° and 19.3°, corresponding to the (110) and (020) planes, respectively, were assigned to CS. Additionally, for the 2wt% of CuO-GO incorporated PVA/CS nanofibrous mats the peaks at 35.50° and 38.55° correspond to the (-111) and (111) planes of CuO. Although the peak at 10.3° is represented by the (002) plane of GO [10].

The degree of crystallinity was determined from the ratio of the area under the main peak to the total area of the diffraction spectrum. The crystallinity of the uncrosslinked and crosslinked PVA/CS nanofibrous mats was found to be 73.13% and 79.41%, respectively. Likewise, the 2 wt% of CuO-GO embedded PVA/CS nanofibrous mats exhibited crystallinity of 66.81% and 75.93% for the uncrosslinked and crosslinked samples, respectively. Generally, from these results, we can confirm the semicrystalline nature of PVA. Furthermore, the loading of CS to form the PVA/CS mats can potentially negatively impact crystallinity since amine groups of CS can interact with the

View Article Online
DOI: 10.1039/D5MA01301A

hydroxyl groups of PVA to form hydrogen bonds, thereby interfering with the formation of PVA crystals.

Interestingly, the 2 wt% of CuO-GO incorporated PVA/CS nanofibrous mats exhibited a slightly lower crystallinity than the PVA/CS mats, denoted by a decrease of about 8.6% and 4.4% for the uncrosslinked and crosslinked samples, respectively. These results were also confirmed by the decrease in peak intensity at around 1146 cm^{-1} in the FTIR spectra (**Figure 3**). It was also noted that the major peaks in the XRD spectra dropped in intensity and broadened with the addition of 2 wt% of CuO-GO NCs. This is a sign of a lowering of the degree of crystallinity, which increases the amorphous nature of the samples. This could be explained by the CuO-GO tiny particles and rigid nature, which interfere with the chain's reorganization and increase ionic conduction because of their potent interaction with PVA/CS [60].

On the other hand, the crosslinking process had a positive effect on the degree of crystallinity. A 6.28% and 9.12% increase was noted for the PVA/CS and the 2 wt% of CuO-GO embedded PVA/CS nanofibrous mat upon thermal crosslinking. This finding suggests an overall enhancement in crystallinity, potentially accompanied by a shift in the crystallization pattern within the amorphous regions. This behavior suggests that the amorphous region between the CuO-GO NCs and the polymer matrix is where the complexation takes place. This enhancement is attributed to thermally induced chain rearrangement and strengthened intermolecular hydrogen bonding between PVA and chitosan, which facilitates the formation of more ordered crystalline regions [48].

3.8 Mechanical properties of nanofibrous mats.

View Article Online
DOI: 10.1039/D5MA01301A

Structural integrity is a vital property of nanofibrous mats used as wound dressings; an ideal dressing material should have physical properties similar to those of natural skin. **Figure 6** shows the typical stress-strain curves, the tensile strength, the Young's modulus, and the elongation at break of the CuO-GO embedded PVA/CS nanofibrous mats. Tensile strength measures the maximum stress a nanofibrous material can withstand under a stretching load. At the same time, modulus is the measure of a material's resistance to elastic deformation when subjected to stress.

As shown in Figure 6a,b, depending on the amount of CuO-GO, the tensile strength gradually increases, reaching 7.08±0.22 MPa at 2 wt% CuO-GO loading, which is about a 182% increase from the tensile strength of the pristine nanofibrous mat. Interestingly, Young's modulus also shows a rise of 839.75% for the same CuO-GO concentration **(Figure 6c)**. The elongation at break of the CuO-GO embedded PVA/CS nanofibrous mats was in the range 9.75-18.01%.

This is an expected situation since GO is a material with high tensile strength and Young's modulus [61]. The rigid CuO NPs were uniformly anchored on the GO surface, thus reducing layer mobility and drastically improving the polymer's mechanical properties. The addition of CuO-GO NC to the PVA/CS polymeric solution had a significant impact on the structure and integrity of the nanofibrous mat, as noted through the IR spectra in **Figure 3**. The intermolecular H-bonds between the OH groups of PVA, CS, and GO were observed. Furthermore, covalent bonding resulting from the ring-opening reaction of epoxy groups in graphene oxide (GO) by the amine groups of chitosan (CS) [62], leading to the formation of amide linkages within the nanofibers, plays a key role in defining the mechanical properties of the CuO-GO embedded PVA/CS nanofibrous mat.

The uniform fiber morphology and nanoscale size distribution provide an additional advantage by contributing to the enhanced tensile strength of the CuO-GO embedded PVA/CS nanofibrous mats. Fiber diameter plays a critical role in determining the tensile properties of nanofibrous materials.

View Article Online
DOI: 10.1039/D5MA01301A

As the diameter decreases to the nanoscale, the unique characteristics of nanofibers begin to dominate. A more uniform and defect-free surface structure allows the fibers to better resist axial tensile forces, leading to enhanced mechanical performance [63]. Furthermore, crosslinking has a direct impact on the mechanical properties of a polymeric system. Thermal crosslinking in the CuO–GO/PVA/CS system is governed by heat-induced dehydration of the PVA phase, which enhances inter- and intramolecular hydrogen bonding between hydroxyl groups, leading to a more compact physically crosslinked network. FTIR confirms this process through a decrease in intensity of the broad O–H stretching band (3200–3500 cm^{-1}), indicating reduced bound water and strengthened hydrogen bonding, along with a more pronounced C–H stretching peak at ~2920 cm^{-1} due to thermal restructuring (**Figure S8a**). The increase in the ~1140 cm^{-1} band (**Figure S8b**) further reflects enhanced ordering of PVA chains, associated with increased crystallinity arising from heat treatment [2][3].

Similar physical trends were observed by Wang et al. [64], who reported that the tensile strength of PVA nanofibers increased sharply by 350%, from 0.5 to 0.75 MPa, upon the incorporation of 8 mg of GO. This enhancement was attributed to efficient load transfer from the polymer matrix to the GO nanosheets. However, at higher GO loadings, the tensile strength gradually reached a saturation point. The incorporation of GO into the PVA matrix also reduced the elongation at break of the composite nanofiber mat, with values decreasing further as the GO content increased from 2 mg to 8 mg. In contrast, Yao et al. [58], reported that the tensile strength of PVA/GO nanofibers is lower than that of pristine PVA nanofibers when the GO content increases beyond a critical threshold (0.4-1 wt%). This variation was ascribed to the influence of the “hydrogen bond barrier” on crystallization at high GO concentrations. Accordingly, the as-prepared PVA/CS nanofibrous mats embedded with a defined wt% of CuO-GO showed an increase in Young’s modulus and

View Article Online
DOI: 10.1039/D5MA01301A

tensile strength consistent with results reported in the literature[64] [58]. Fundamentally, the design and manufacture of wound dressing scaffolds should ensure that the employed materials demonstrate unique mechanical (i.e., flexibility, softness, permeability, and elasticity) and biochemical (i.e., biocompatibility and biodegradability) properties that allow for comfort and functionality in treating wounds. Flexible substrates such as nanofibrous mats can also allow for the integrated sensors to adapt to irregular wound surfaces without causing discomfort [65].

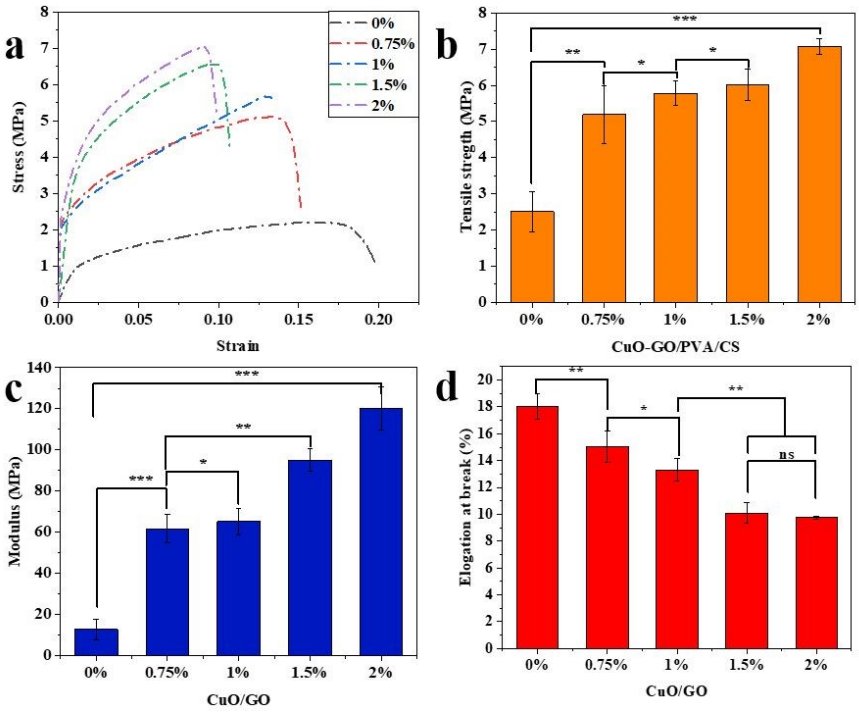

Figure 6. Mechanical properties of different wt% of CuO-GO loaded PVA/CS nanofibrous mats and pristine PVA/CS nanofibrous mat; (a) stress-strain curves, (b) tensile strength, (c) tensile modulus, and (d) elongation at break. n= 3. The results are presented as the mean ± standard deviation (SD). The significance levels denoted as follows: *p ≤ 0.05, **p ≤ 0.01, and ***p ≤ 0.001.

3.9 Porosity of nanofibrous mats

View Article Online
DOI: 10.1039/D5MA01301A

Nanofibrous mats possess a structural similarity to the extracellular matrix, making them highly attractive scaffolds for wound healing applications. Among their critical properties, porosity plays a central role, as it directly influences oxygen and nutrient transport, exudate absorption, and cell infiltration. Porosity is defined as the percentage of void space in a solid sample, and in this study, it was determined using the gravimetric method. In this approach, samples were weighed dry, soaked in ethanol to fill the pore volume without altering the fiber structure, and then reweighed. Porosity was subsequently calculated based on the weight difference and the bulk density of ethanol relative to the apparent density of the mat.

In Figure 7a, the porosity of the nanofibrous mats was plotted against the concentration of embedded CuO-GO NCs. The 0.75 wt% of CuO-GO embedded PVA/CS nanofibrous mats exhibited porosities ranging between 83.28 ± 3.8% and 2 wt% CuO-GO embedded nanofibrous mats showed 77.25 ± 4.9%, however, pure PVA/CS mat showed a much lower porosity of 74.5 ± 2.5%. The observed trend reflects a strong correlation between porosity and fiber morphology. As the CuO-GO content increased, the nanofibers transitioned from larger, well-spaced linear fibers to thinner, compressed, and wavy structures, as confirmed by SEM analysis **(Figure 5**). This morphological change affects packing density and fiber orientation, leading to reduced pore volume. Interestingly, the incorporation of CuO-GO improves electrical conductivity while lowering viscosity (**Figure 2**), resulting in thinner fibers, which would normally lower porosity. The inherently rough and irregular surface of the CuO-GO particles offsets this effect to some extent, contributing to increased pore formation. Thus, optimizing CuO-GO concentration is essential to balance porosity, fiber diameter, and structural stability.

Porosity of the as-prepared nanofibrous mats (77-83%) falls within the ideal range for wound dressing materials, which is generally 60-90% [66]. Porosity above 90% can compromise

View Article Online
DOI: 10.1039/D5MA01301A

mechanical stability and increase brittleness, leading to fluid leakage. Porosity below 60% can hinder oxygen and nutrient transport, impairing wound healing.

The relationship between fiber diameter and porosity observed here is consistent with previous reports on rGO loaded PVA fiber by Gozutok et al. [67]. They reported that the rGO-(0.5 and 1%.) loaded PVA nanofiber had a porosity of 81.6% while pure PVA had a porosity of 79.4%. Further, an increase of rGO to 1% of decrease in porosity of the mat. Additionally, thermal crosslinking performed at 120 °C for 80 min further modified the mats, as confirmed by FTIR (**Figure 3**). Thermal crosslinking reduces porosity by inducing the loss of intra- and interstitial water, leading to fiber shrinkage and fusion, thereby densifying the nanofibrous mats. This accentuates the multifaceted chemistry of fibers composition, morphology, and post-processing conditions in tailoring porosity to meet the requirements of effective wound dressings.

3.10 Wettability analysis of nanofibrous mats

The wettability of the CuO-GO embedded PVA/CS nanofibrous mats was evaluated by water contact angle (WCA) measurement (**Figure 7b**). WCA is a reliable indicator of a material's surface hydrophilicity, offering valuable insights into its surface chemistry and suitability for wound dressing applications.

Both PVA and CS are inherently hydrophilic due to the abundance of functional groups capable of hydrogen bonding. PVA contains numerous -OH groups, while CS contributes -NH_2 and -OH groups, resulting in a strong affinity for water molecules. Accordingly, the pristine PVA/CS nanofibrous mat exhibited a low WCA of 38.6°, reflecting its high hydrophilicity [49]. .

Upon incorporating CuO-GO nanocomposites, the water contact angle increased progressively with loading concentration. The 0.75, 1.0, 1.5, and 2.0 wt% of CuO-GO embedded PVA/CS

View Article Online
DOI: 10.1039/D5MA01301A

nanofibrous mats exhibited WCAs of 44.8°, 48.2°, 52.3°, and 64.4°, respectively. This trend indicates a reduction in surface hydrophilicity with increasing nanofiller content. Similar observations reported by Dubey et al. [15] demonstrated that the incorporation of PEGylated GO into PVA/CS nanofibers increased the WCA from 27° (pristine PVA/CS) to 58°, attributing the effect to the amphiphilic nature of GO, where the hydrophobic basal plane reduces water affinity.

Interestingly, Sandra et al. [12], reported that CuO incorporation alone did not significantly alter the hydrophilicity of PVA/CS nanofibers. In contrast, Parvinnasab et al. [68] found that copper complexes improve hydrophilicity. This increase is attributed to the influence of copper complexation on chitosan crystallinity and the occupation of hydrophilic functional groups, such as hydroxyl and amino groups [68]. The combined effects of both CuO and GO may be responsible for the more pronounced increase in WCA observed in this study. Overall, while the incorporation of CuO-GO reduces the hydrophilicity of the nanofibers, the mats remain sufficiently wettable to support cell adhesion and proliferation. This moderate hydrophilicity is advantageous, as it not only provides a favorable platform for cellular interactions but also facilitates controlled release of CuO-GO nanocomposites into the wound bed.

3.11 Swelling and water uptake analysis of nanofibrous mats

The water uptake capacity of the thermal crosslinked nanofibrous mats was determined using PBS solution at pH 7.4, to simulate wound exudates. The experiment was conducted over 3 days, during which the nanofibrous mats gradually lost weight upon reaching equilibrium.

In Figure 7c, the PVA/CS nanofibrous mat exhibited an equilibrium swelling percentage of approximately 475%, indicating its strong fluid absorption capacity. The swelling profile revealed rapid fluid uptake within the first 12 h, followed by a gradual decrease up to 72 h. In contrast, the

View Article Online
DOI: 10.1039/D5MA01301A

incorporation of CuO-GO nanocomposites into the PVA/CS nanofibers resulted in reduced swelling percentages. The 0.75 wt% of CuO-GO embedded PVA/CS nanofibrous mat reached an equilibrium swelling of 433%, while higher CuO-GO loadings further decreased swelling to 420%, 404%, and 381% for the 1.0, 1.5, and 2.0 wt% formulations, respectively. This reduction can be attributed to the decreased availability of free hydroxyl groups during blending, as more CuO-GO interacts with PVA and CS chains, limiting water uptake. Similar results were reported by Liu et al. [69] their study showed that the equilibrium water absorption of the PVA/CS nanofiber mat prepared via solution blowing varies from 680 to 459% depending on the content of the crosslinker.

Furthermore, all nanofibrous mats reached equilibrium swelling within 12 h, except for the 0.75 and 1.0 wt% CuO-GO embedded PVA/CS nanofibrous mats, which took 24 h to reach equilibrium. After reaching equilibrium, the swelling gradually decreased for the remaining period of the study. The reduction in swelling can be attributed to the release of the entrapped CuO-GO NCs. Despite the reduction, all CuO-GO embedded PVA/CS nanofibrous mats still demonstrated very high swelling capacity, confirming their hydrophilic nature and suitability for wound dressing applications. The high porosity (Figure 7a), along with the abundant oxygen-containing groups in PVA, CS, CuO and GO, provided numerous sites for hydrogen bonding with water molecules. Additionally, the large surface area of the nanofibers ensured greater exposure to PBS, further facilitating water absorption.

Another important factor, such as thermal annealing, enhanced the stability of the nanofibrous mats by increasing crosslinking density [70]. In PVA/CS mats, annealing promoted hydrogen bonding between the OH and NH_2 groups of chitosan and OH groups of PVA hydroxyls, reducing polymer free volume and swelling. In CuO-GO embedded PVA/CS mats, GO provided additional crosslinking sites; epoxide groups formed C–N linkages with chitosan's amine moieties, and

View Article Online
DOI: 10.1039/D5MA01301A

carboxyl groups reacted with amines under heat, further strengthening the network [62]The reduced swelling ratio of the annealed CuO-GO embedded PVA/CS mats is attributed to GO-mediated crosslinking.

3.12 Degradation Assessment of nanofibrous mats

Biodegradation of nanofibrous wound dressing mats is necessary and should be matched with the wound healing periods. Polymeric biodegradable mats partially dissolve when in contact with the wound fluid, and this process leads to the formation of a soluble hydrophilic gel that protects the wound and stimulates the granulation and epithelialization [49]. In this study, the *in vitro* degradation of thermally stabilized CuO-GO embedded PVA/CS nanofibrous mats was evaluated in PBS (pH 7.4) at 37 °C over an interval of 3 weeks (**Figure 7d**). The results showed that all prepared formulations lost nearly half of their original mass within the first week. The bare PVA/CS nanofibrous mat exhibited the fastest degradation, losing approximately 52% of its weight during the first week and leaving behind only 10% of its initial weight by the end of the third week.

Comparable findings have been reported by Victor et al. [71], who observed that the degradation of the PVA-based nanofibers with high chitosan content was much pronounced, with a weight loss of about 50% after one week. CS has a large amount of NH_2 and OH fuctional groups that are responsible for increasing the affinity with aqueous solutions by forming hydrogen bonds. In contrast, the incorporation of CuO-GO markedly improved the stability of the mats in a concentration-dependent manner. Among the tested samples, the 2 wt% of CuO-GO embedded PVA/CS nanofibrous mat demonstrated the highest stability, retaining 22% of its initial mass after three weeks. This stabilization effect can be attributed to the enhanced crosslinking density imparted by the CuO-GO, PVA, and CS network.

View Article Online
DOI: 10.1039/D5MA01301A

Interestingly, the lower degradation of the CuO-GO-loaded mats compared to pristine PVA/CS can be explained by the absence of free amine and hydroxyl groups, since most of them are used up in forming crosslinking networks with the CuO-GO NCs and the polymer matrix. Additionally, the thermal stabilization process carried out at 120 °C for 80 min was sufficient to induce PVA crystallization, enhance fiber densification, and thereby prolong fiber stability in solution[72].It can be stated that the wound dressing mat could survive the physiological environment and offer an adequate template for tissue regeneration during the wound healing periods.

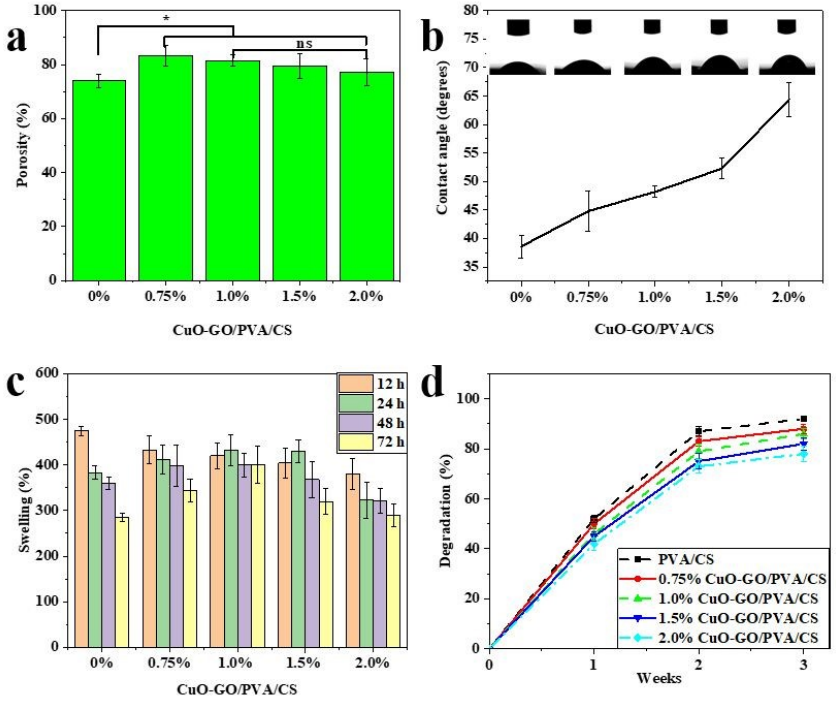

Figure 7. Physicochemical properties of CuO-GO/PVA/CS nanofibrous mats: (a) porosity percentage, (b) static water contact angle, (c) swelling ratio over time, and (d) *in vitro* degradation profile. All measurements were conducted in triplicate, and data are presented as mean ± standard deviation. The significance levels denoted as follows: *p ≤ 0.05.

3.13 Cytotoxicity test of nanofibrous mats

View Article Online
DOI: 10.1039/D5MA01301A

The potential risks arising from the interactions of the CuO-GO embedded PVA/CS nanofibrous mat with living tissue must be evaluated during wound dressing design. In the present study, CuO-GO NCs were synthesized at a 1:1 ratio (CuO:GO) and incorporated into PVA/CS nanofibers at concentrations ranging from 0.75% to 2%. The Vero cells were cultured in the extract solutions of the PVA/CS nanofibrous mats, and the cytotoxicity was estimated by determining the viable cell densities under an inverted light microscope after 48 h **(Figure 8).**

To evaluate the *in vitro* cytotoxicity, the effect of CuO-GO embedded PVA/CS nanofiber mats on the proliferation of Vero cells was tested. As shown in **Table 2**, the 0.75, 1, 1.5, and 2 wt% of CuO-GO embedded PVA/CS nanofibrous mats had no significant influence on the proliferation of Vero cells compared to the control groups, with results showing >95% of cell survival. The cytotoxicity of CuO and GO is highly dependent on their concentration and particle size. Wang et al. [73] reported that GO concentrations below 2 wt% were non-toxic to human fibroblasts, whereas higher loadings above 5 wt% induced dose-and time-dependent cytotoxicity, with effects such as reduced adhesion, apoptosis, and nuclear internalization. Bhattacharya et al. [74] further reported that CHO cells retained 86% of viability at 2.5% of CuO NP concentration, but survival sharply decreased to 55% at 3%, indicating a narrow therapeutic window. Importantly, concentrations below 2.5% did not cause major morphological changes in cells and were considered safe for biomedical use. Taken together, these studies showed that both graphene oxide and copper oxide exhibit beneficial therapeutic properties at low concentrations but may exert cytotoxic effects at higher doses. Our results suggest that controlled loading of CuO-GO within nanofibrous mats not only preserves biocompatibility but also provides a safer and more effective wound-healing platform by regulating nanoparticle exposure. Further, the embedded CuO-GO within a nanofibrous mat minimizes risks associated with nanoparticle aggregation and

View Article Online
DOI: 10.1039/D5MA01301A

uncontrolled local concentrations, which are often reported when metal-based nanoparticles are applied directly to wound surfaces. The polymeric nanofiber matrix, therefore, acts as a protective carrier, ensuring gradual and controlled release of CuO-GO into the wound bed while retaining its wound-healing efficacy.

Table 2. Evaluation of the cell viability of Vero cells

Sample ID	**Cell survival (Vero cell)**	**Remarks**
Solvent -	100%	No Cytotoxicity was observed on the Vero cell line
Solvent +	95±5.3	
0.75% CuO-GO embedded	95±3.6	
1.0% CuO-GO embedded	95±2.4	
1.5% CuO-GO embedded	95±2.8	
2.0% CuO-GO embedded	95±0.9	

View Article Online
DOI: 10.1039/D5MA01301A

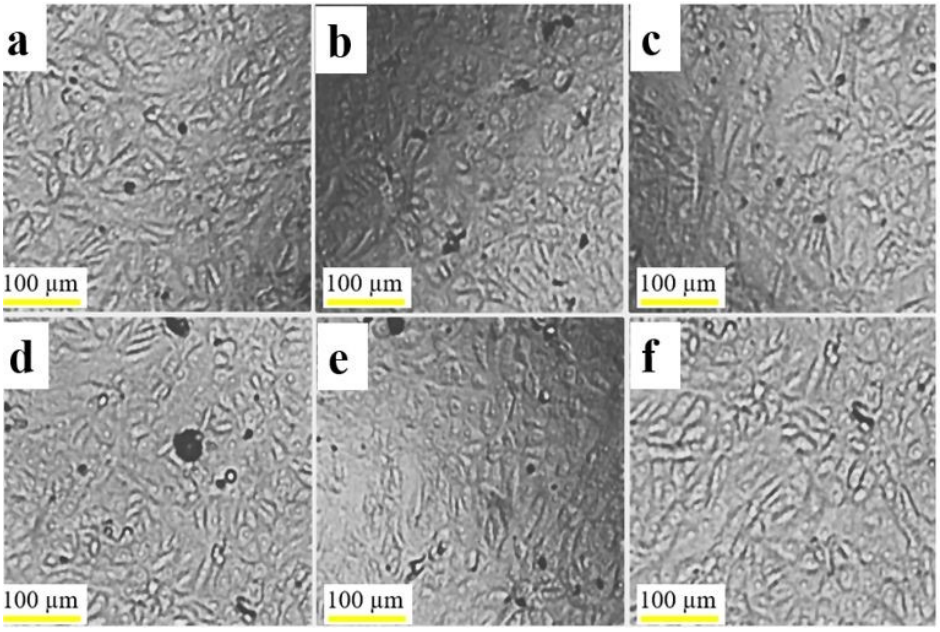

Figure 8. Light microscope images of Vero cells treated with electrospun CuO-GO/PVA/CS nanofibers at concentrations of 0.75%, 1.0%, 1.5% and 2.0 wt% CuO-GO NC (a-d), while (e and f) are the positive and negative controls, respectively. Scale bar =100 µm.

3.14 Hemocompatibility of nanofibrous mats

The CuO–GO/PVA/CS nanofibrous mats exhibited very low hemolysis rates of 1.25 ± 0.9%, 2.91 ± 1.5%, 3.37 ± 1.9%, and 4.25 ± 2.5% for increasing CuO–GO content, respectively, all remaining below 5% (**Figure 9a**). These results confirm excellent hemocompatibility with negligible red blood cell damage, as visually supported by the clear supernatants compared to the bright red positive control (**Figure 9b**). The slight increase with higher CuO-GO loading suggests marginally enhanced cell–material interaction, but still within safe limits for biomaterial applications. This low hemolytic behavior aligns with ISO 10993-4 standards. Moreover, the BCI values after 3 min were 23.30 ± 2.5%, 21.18 ± 1.9%, 15.25 ± 1.4%, and 15.25 ± 2% for 0.75%, 1.0%, 1.5%, and 2.0% of CuO–GO/PVA/CS mats, respectively, indicating progressively enhanced clot formation

View Article Online
DOI: 10.1039/D5MA01301A

with increasing CuO–GO content (**Figure 9c and d).** Lower BCI values reflect faster coagulation compared to the control, confirming improved hemostatic activity. This behavior suggests that the nanofibrous surface promotes protein adsorption and platelet activation, accelerating fibrin network formation. The trend is consistent with literature reporting that chitosan enhances hemostasis through electrostatic interaction with blood components and platelet aggregation, while graphene oxide contributes through hydrophilic oxygenated groups and surface charge–mediated platelet activation [75][76].

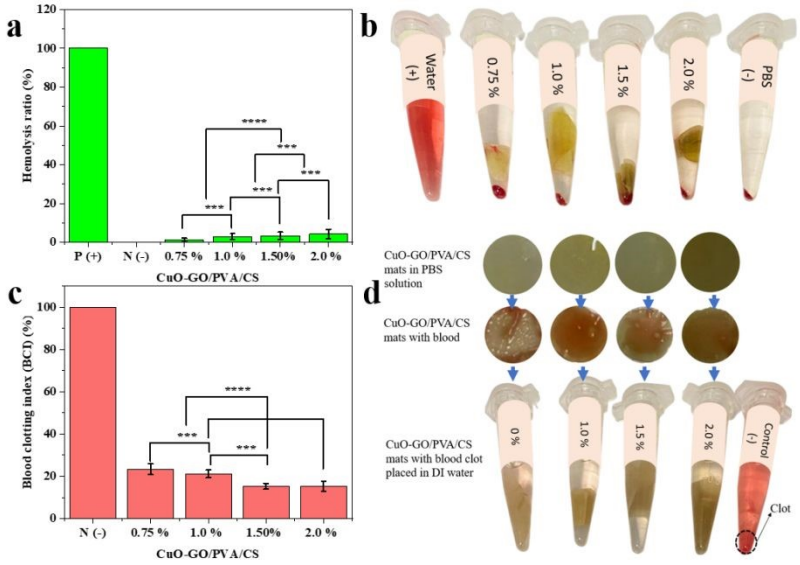

Figure 9. (a) Hemolysis assay for various electrospun nanofibrous mats expressed in terms of hemolytic ratio, (b) represents photographs of various electrospun samples and controls after centrifugation, (c) quantitative statistics of the blood clotting index of the nanofiber mats, (d) pictures of the BCI. Data are expressed as mean ± SD.***P < 0.001, and ****P < 0.0001 (n = 3).

3.15 *In vivo* wound healing study of nanofibrous mats.

The wound healing process was investigated by measuring and comparing the average wound area in different groups on the 1st, 2nd, 7th, and 14th day (**Figure 10a**). *In vivo* studies are essential for

View Article Online
DOI: 10.1039/D5MA01301A

evaluating the actual wound healing efficacy of biodegradable electrospun nanofibrous mats under physiological conditions. In this study a full-thickness skin defects of diameter 2 cm were treated with 2wt% of CuO-GO embedded PVA/CS nanofibrous mat, while the control group was left open.

Wound healing is initiated following skin injury and involves a complex interplay of various cell types, cytokines, structural proteins, and growth factors that work together to restore tissue integrity. The 2wt% of CuO-GO embedded PVA/CS mat treated wounds were able to achieve 100% of wound closure by day 14. More interestingly, on day 2 and 7 post injury, the 2wt% of CuO-GO embedded PVA/CS mat treated wound closure was 48.83 ± 3.7 and 82.51±1.6%, respectively, as seen in **Figure 10b**. Recent investigations have demonstrated that electrospun nanofibrous mats incorporating copper NPs promote rapid early-phase wound contraction *in vivo* [77]. The control group exhibited 35.39 ± 0.8 and 62.61 ± 2.3% of wound closure, respectively, within a similar period. To ascertain the significance of the treatment, the control and 2wt% of CuO-GO embedded PVA/CS nanofibrous mats treated groups were analyzed using an ANOVA test. There is a significant decrease in the average wound area on the 2^{nd}, 7^{th}, and 14^{th} days in the recipient groups of the nanofibrous mat-treated compared to the negative control group. Visual inspection of the wound on day 2, as seen in the optical images in **Figure 10a**, revealed the presence of serous exudate and redness around the wound in the control mice, indicating inflammation. Compared to the nanofibrous mat-treated groups, where the wound area was uniformly moist with no visible signs of inflammation. Enhanced tissue regeneration was evidenced by the early appearance of hair follicles, neovascularization, and sebaceous gland features, which were less pronounced in control groups. The synergistic interaction of these components culminated in an accelerated healing process.

View Article Online
DOI: 10.1039/D5MA01301A

The excellent swelling ability of the nanofibrous mat ensured absorption of wound exudate, which can facilitate keratinocyte migration. Furthermore, CuO has been shown to possess anti-inflammatory properties [78]. By modulating the inflammatory response, CuO-GO can help reduce excessive inflammation and promote a more favorable environment for wound healing.

Recent studies have demonstrated that copper-containing wound dressings can accelerate wound healing, stimulate neovascularization, and enhance keratinocyte activity. Lin et al. [79] fabricated coaxial nanofiber mats with a unique "core/sheath" structure consisting of CuO_2-PVP composite sheath and a PCL core. The system allowed for the slow dissolution of the PVP at the wound side, releasing the CuO_2 at the wound bed, effectively suppressing inflammation while promoting angiogenesis. Cell attachment analysis showed that fibroblast cells had migrated and expanded well in the nanofibrous structures.

Figure 10c. depicts the proposed wound healing mechanism, facilitated by CuO-GO embedded PVA/CS nanofibrous mat. An *in vivo* study using Swiss Albino mice demonstrated the efficacy of the CuO-GO embedded PVA/CS nanofiber mat in enhancing wound healing. The biodegradable 3D nanofibrous mat accelerates wound contraction through the synergistic effects of its bioactive components. This integrated framework promotes rapid tissue closure by combining the structural advantages of the nanofibers with the therapeutic properties of the embedded agents [80]. First, the gradual degradation of the nanofiber matrix enabled sustained release of the CuO-GO nanocomposite into the wound bed. The release of CuO-GO plays an important role in epithelial cell migration and blood coagulation, promoting wound healing by encouraging angiogenesis and enhancing proliferation of fibroblasts, and facilitating collagen deposition [81] Second, the numerous OH functional groups of PVA, CS, and GO impart hydrophilic properties to the mat, allowing it to absorb and store wound exudates, keeping the wound area moist. Moreover, the

View Article Online
DOI: 10.1039/D5MA01301A

mat's high porosity facilitated efficient exudate uptake, preserving a moist wound environment. A significant reduction in macrophage infiltration signaled the transition from inflammation to the proliferative phase. The moist wound condition is suitable for cell migration and proliferation. CS can rapidly stop hemorrhage by binding to red blood cells, initiating early blood clotting. Furthermore, CS regulates inflammatory cells, encouraging granulation and organization. Graphene oxide provided a bio-adhesive surface conducive to cellular adhesion and proliferation. Third, the nanofibrous mat was broken down by the body's metabolic system, and the residues were bioabsorbed, allowing for wound healing without debridement and changing the dressing [82].

We reported the fabrication of PVA/chitosan electrospun mats incorporating a graphene oxide–copper oxide (GO-CuO) nanocomposite, offering a chemically stable, cost-effective, and storage-robust platform with strong clinical translation potential. The GO sheets act as carriers and stabilizers for copper, preventing nanoparticle aggregation and enabling controlled copper ion release below cytotoxic thresholds, while leveraging copper's bioactive antimicrobial and wound-healing properties, including promotion of angiogenesis and collagen deposition[65]. The combination of GO and copper also enhances mechanical stability, improves nanofiber dispersion, and provides a synergistic platform that supports tissue regeneration. Coupled with the scalability of electrospinning, sterilization compatibility, and regulatory familiarity of PVA and chitosan, this system represents a highly practical and multifunctional approach for advanced wound management and broader clinical deployment.

View Article Online
DOI: 10.1039/D5MA01301A

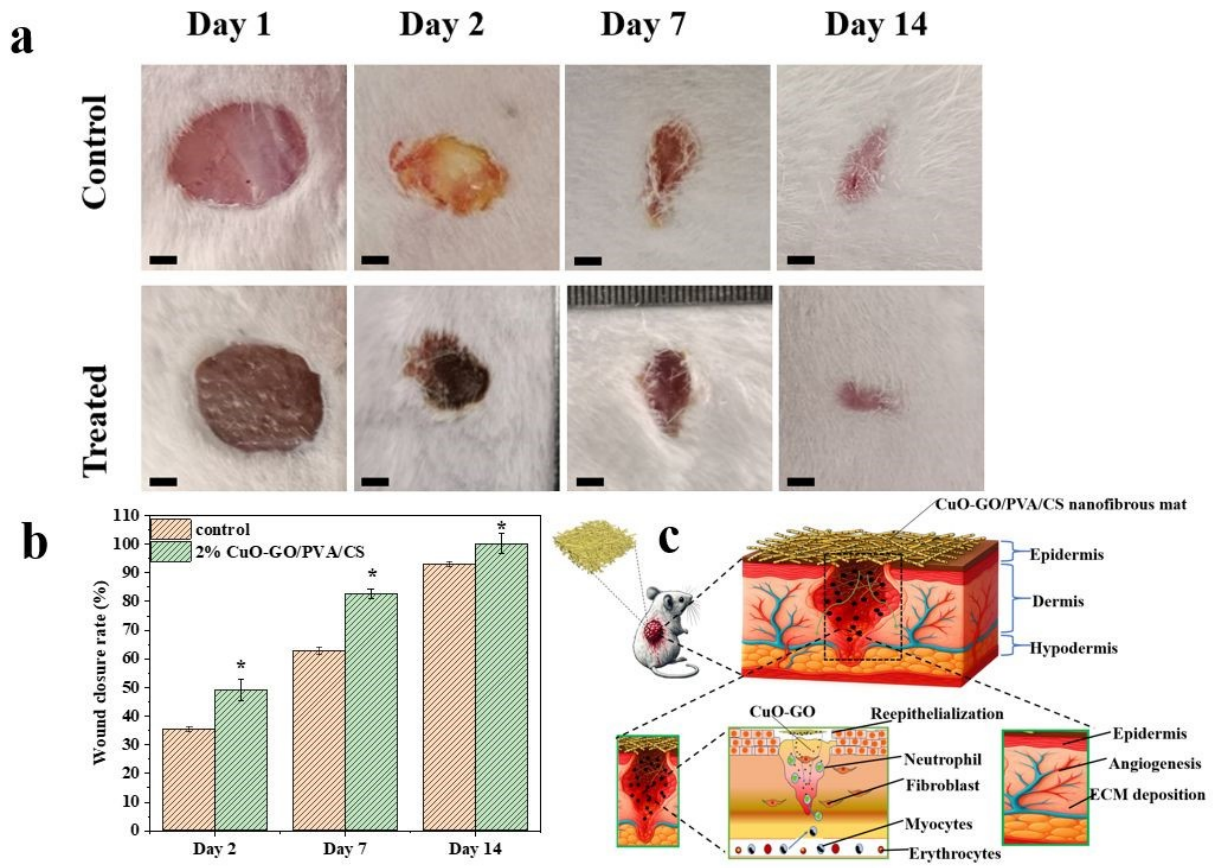

Figure 10. Comparative analysis of wound healing efficiency in Swiss albino mice (a) Photographs displaying the condition of wounds at different time intervals, over 14 days, scale=5mm (b) Graph representation of the reduction in wound area for the 2 wt% of CuO-GO embedded PVA/CS mats and untreated control at various time points. All in vivo experimental procedures were independently replicated 3 times (n = 3), and the results are presented as the mean ± standard deviation (SD). The significance levels denoted as follows: *$p \leq 0.05$. (c) wound healing mechanism.

3.16 Histopathology study

To get a better insight into the wound-healing properties of the 2 wt% of CuO-GO embedded PVA/CS nanofibrous mat, a histopathological study based on Hematoxylin and Eosin (H&E), and

View Article Online
DOI: 10.1039/D5MA01301A

MT staining was carried out to assess the extent of re-epithelialization, granulation tissue formation, and collagen deposition. Tissue biopsies were collected from the wound site on days 2, 7, and 14.

H&E staining was executed on tissue sections obtained on days 2, 7, and 14 following wounding. (**Figure 11a**). On day 2, skin tissues taken from the wound sites of the control and the 2 wt% CuO-GO embedded PVA/CS nanofibrous mat-treated groups displayed a disrupted epidermal and dermal layer. Inflammatory cells (microphages and neutrophils) were seen to migrate to the wound site, where they function to clear debris, secrete cytokines, and orchestrate tissue repair [72]. Moreover, the mat-treated wounds exhibited abundant macrophage infiltration, suggesting early migration and more efficient inflammatory transition. By day 7, dense fibroblast cells and thick, abundant granulation tissue can be observed in the 2 wt% of CuO-GO embedded PVA/CS nanofibrous mat-treated wounds. Additionally, numerous new blood vessels (angiogenesis) and hair follicles were visible in the dermal layer, with the regenerated epidermis being thin. However, wounds in the control group showed less amount of newly formed tissue, exhibiting sparse fibroblast infiltration and disorganized granulation tissue. The presence of inflammatory cells was also noted (arrow labeled M). Furthermore, the negative control group displayed minimal follicular regeneration and hair growth, related to poor wound healing and tissue regeneration [80].

After 14 days, the wounds in the control and 2 wt% of CuO-GO embedded PVA/CS mat-treated group showed good signs of healing, with a thickened epidermis covering the tissue surface. Furthermore, the nanofibrous mat-treated group exhibited a compact dermis, including blood vessels and hair follicles, highlighting the as-prepared nanofibrous mat's ability to promote rapid and organized tissue regeneration. The H&E staining results suggested that wounds treated with 2 wt% of CuO-GO embedded PVA/CS nanofibrous mat can achieve relatively sufficient healing

View Article Online
DOI: 10.1039/D5MA01301A

through early immune modulation, improved fibroblast and keratinocyte activity, and enhanced tissue remodeling [83].

In addition, collagen fiber deposition was assessed by MT staining of the tissue samples taken from the wound site, as shown in **Figure 11b**. On day 2, both the control and 2 wt% CuO-GO embedded PVA/CS mat-treated groups exhibited disrupted dermal-epidermal junctions and fewer collagen fibers at the wound edge, indicative of acute injury and the early inflammatory phase. However, the mat-treated wound revealed comparatively greater cellular infiltration and early fibroblast activation, with loosely arranged collagen strands beginning to appear around the wound bed, suggesting accelerated ECM deposition. By day 7, a clear difference between the control and the nanofibrous mat-treated wound was noted. The control wound depicted aligned collagen parallel to the skin, with diffuse and uneven blue collagen staining, and minimal granulation tissue formation (arrow labeled C-aligned). Conversely, the as-prepared nanofibrous mat-treated wound displayed a denser collagen network with prominent dermis formation. Dermal appendages, such as nascent hair follicles and sebaceous gland-like structures, were evident in the treated tissue, indicating regenerative rather than merely reparative healing. This suggests enhanced fibroblast proliferation, increased myofibroblast activity, and an accelerated transition into the proliferative phase enabled by the bioactive nanofibrous mats. On day 14, the 2 wt% of CuO-GO embedded PVA/CS mat-treated group exhibited nearly complete tissue remodeling through continuous, stratified epithelium and a well-integrated collagen matrix filling the wound bed. The collagen was densely packed with a basket-weave pattern, as evidenced by deeper and more uniform blue staining (arrow labeled C-not aligned). Notably, the incorporation of CuO-GO NC endowed the mat with excellent, rapid wound-healing properties. Moreover, GO could activate the clotting factors [84] , which noticeably accelerates scab formation at the wound site. Hussein et al. reported

View Article Online
DOI: 10.1039/D5MA01301A

that GO could serve as an outstanding artificial extracellular matrix supporting cell attachment and proliferation due to its honeycomb structure [85]. GO-incorporated mat could down-regulate scar-related gene expression, and it could potentially facilitate scar-free wound closure [86]. Therefore, GO is an emerging biomaterial for wound healing with promising therapeutic advantages. The oxygen-containing functional groups on the surface of GO create a hydrophilic character, enabling dispersibility, chemical modifications, and loading therapeutic components through both noncovalent interactions and covalent bonds via chemical reactions. In this study, the GO was decorated with CuO to offer synergistic properties of both GO and CuO. During the inflammatory stage, CuO can block the production of pro-inflammatory substances like interleukin-1 beta and tumor necrosis factor-alpha within neutrophils [87]. Leading to the release of soothing substances such as interleukin-10 and transforming growth factor-beta (TGF-β). Excessive inflammation can obstruct the formation of new blood vessels, disrupt the choreographed movements of cells essential to wound healing, and impede the production of critical components of the extracellular matrix. Furthermore, CuO promoted angiogenesis and collagen cross-linking, evidenced by the dense dermal cellularity and organized ECM seen by day 7. Moreover, the wounds demonstrated features indicative of the remodeling phase, such as the presence of a fully differentiated epidermis with visible rete ridges, aligned collagen fibers in the dermis, and signs of appendage regeneration, which were largely absent in the control group by day 14. These findings suggest not only accelerated wound closure but also the potential for functional tissue restoration. The reduced inflammatory burden and organized tissue structure seen in the nanofiber group imply a lower risk of chronic wound development and scarring.

When compared to conventional wound management strategies, which often fail to resolve inflammation or stimulate sufficient tissue remodeling, the as-prepared nanofibrous mat-based

View Article Online
DOI: 10.1039/D5MA01301A

treatment offers a multifunctional approach. The nanostructured topography of the mat mimics native ECM, facilitating cell adhesion and directional migration; its controlled degradation may provide sustained release of bioactive ions and oxygen species that promote tissue regeneration. Its ability to modulate the immune response, support granulation tissue formation, and expedite epidermal regeneration positions it as a promising candidate for clinical translation in the management of acute and potentially chronic wounds compared with conventional wound dressings. Furthermore, these nanofibers induce less inflammation and permit fast transition to proliferation and neogenesis of vital structures at the wound site, thereby speeding up tissue remodeling. Additionally, these materials can be used to fabricate various designs with many shapes to lessen severe compression on nerve tissue after implantation. These findings suggest that the CuO-GO embedded PVA/CS nanofibrous mat could be highly beneficial in treating complex wounds, such as diabetic ulcers, burns, and surgical incisions, where delayed healing and frequent changing of dressing materials are major concerns. Though the CuO-GO-loaded PVA/CS electrospun nanofibrous mats reported in this study represent an efficient approach to maintaining the biological activity of the wound dressing. Embedding CuO-GO NCs within the nanofibers prevents discharge by wound exudate, allowing a sustained release that aligns with the mat's degradation rate. Thus, efficiently manages inflammation and accelerates the wound's transition into the proliferation phase for enhanced healing. Several outstanding questions remain before clinical translation is guaranteed. Importantly, the safety of using CuO-GO embedded PVA/CS nanofibrous mats for treating wounds is supported by various factors. First, the matching degradation rate of the nanofibrous mats to the wound closure limits the possibility that nanoparticles would leak into the blood system and target other organs. Second, from the *in vivo* cytotoxicity assays, our studies have shown that the CuO-GO embedded nanofibrous mats are

View Article Online
DOI: 10.1039/D5MA01301A

nontoxic. Third, the chitosan and PVA used in this study are generally recognized as safe and approved by the FDA as essential materials already widely applied in the clinic. Compared to other wound healing concepts (Table S1), we present PVA/CS electrospun nanofibrous mats incorporating CuO-GO NCs, offering a chemically stable, and storage-robust platform with strong clinical translation potential.

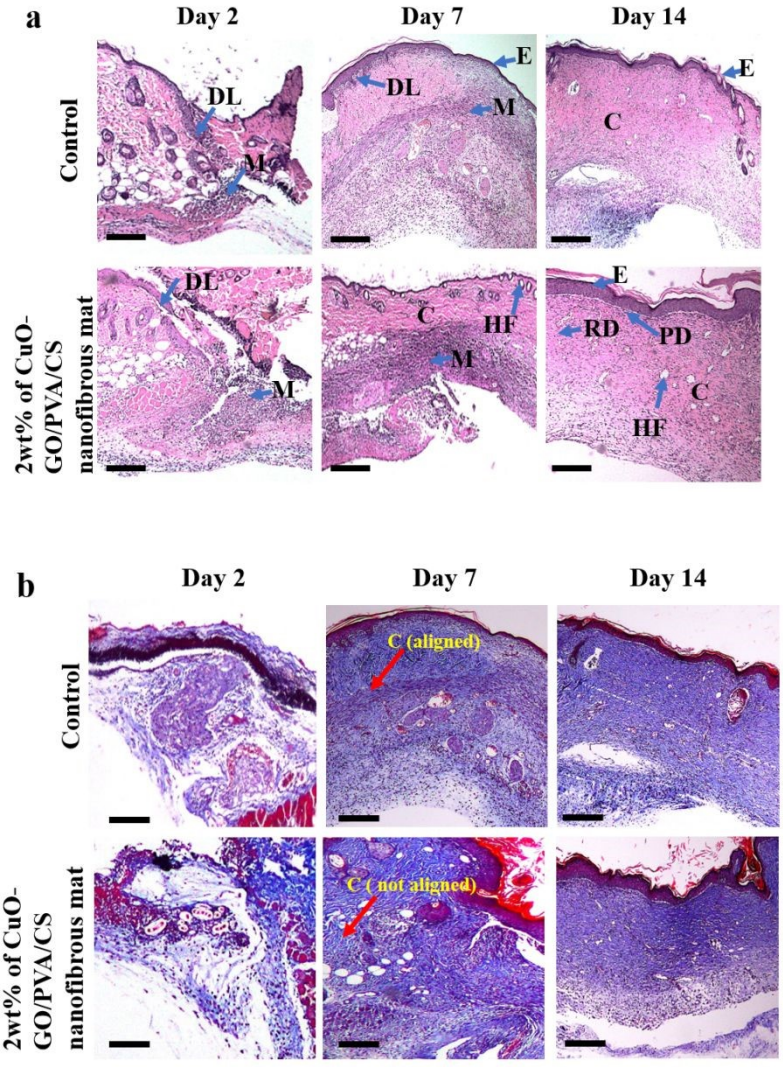

View Article Online
DOI: 10.1039/D5MA01301A

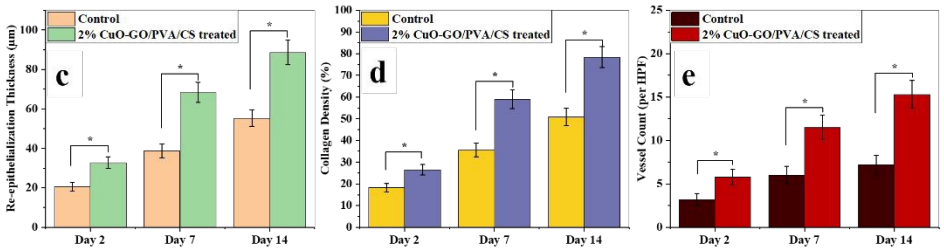

Figure 11. Histological images of untreated (control) and 2wt% of CuO-GO embedded PVA/CS-treated wounds at 2, 7 and 14 days post injury. Evaluation of tissue sections was performed under a bright-field optical microscope. (a) Hematoxylin and Eosin (H&E) staining and (b) Masson's trichrome (MT) staining. (scale bar=50 μm). Histomorphometric analysis of wound healing parameters. (c) Re-epithelialization thickness measured across the regenerated epidermal layer; (d) collagen density quantified within the dermal matrix; and (e) neovascularization expressed as vessel count per high-power field (HPF). Data are presented as mean ± standard deviation (SD). Statistical analysis was performed using one-way ANOVA comparing control and treated groups, with significance defined at *p < 0.05.

3.17 Histomorphometry analysis

The results of histomorphometry analysis are presented as plots in **Figure 11(c-e)** demonstrated a progressive and biologically consistent enhancement of wound healing in the 2wt% of CuO-GO embedded PVA/CS-treated group across all evaluated parameters. At Day 2, the control group exhibited limited tissue regeneration, with re-epithelialization of 20.5 ± 2.1 μm (**Figure 11c**), collagen density of 18.2 ± 2.0% (**Figure 11d**), and vessel density of 3.2 ± 0.7/ HPF (**Figure 11e**). In comparison, the treated group showed improved healing responses, with re-epithelialization increasing to 32.8 ± 3.0 μm, collagen deposition to 26.5 ± 2.4%, and vessel density to 5.8 ± 0.9/ HPF, indicating an accelerated transition from the inflammatory to the proliferative phase. By Day 7, the treatment effect became more pronounced, as the

View Article Online
DOI: 10.1039/D5MA01301A

treated wounds reached 68.4 ± 5.1 μm re-epithelialization, 58.9 ± 4.3% collagen density, and 11.5 ± 1.4/HPF vessel count, whereas the control wounds showed more moderate healing progression with values of 38.7 ± 3.5 μm, 35.6 ± 3.2%, and 6.0 ± 1.0/HPF, respectively. At Day 14, the treated group demonstrated near-complete wound healing, characterized by re-epithelialization of 88.7 ± 6.2 μm, collagen density of 78.4 ± 4.8%, and vessel density of 15.3 ± 1.6/HPF, reflecting advanced tissue remodeling and maturation. Meanwhile, the control group remained lower, with re-epithelialization of 55.3 ± 4.2 μm, collagen density of 50.8 ± 4.0%, and vessel density of 7.2 ± 1.1/HPF. Overall, the coordinated increase in epithelial regeneration, extracellular matrix deposition, and angiogenesis confirms that 2wt% of CuO-GO embedded PVA/CS nanofibrous mats accelerate multiple stages of wound healing, resulting in faster and higher-quality tissue repair while maintaining physiologically plausible healing kinetics.

4. CONCLUSIONS

CuO nanoparticles stabilized with chitosan were synthesized via a green chemistry route, employing chitosan as both a reducing and stabilizing agent. Freshly prepared CuO decorated GO nanocomposite was prepared by ultrasonication process. Then varying wt% of CuO-GO incorporated poly(vinyl alcohol)/chitosan nanofibrous nonwoven mats fabricated through the electrospinning process. Scanning electron microscopy (SEM) analysis confirmed the formation of uniform, bead-free nanofibrous architectures with narrower fiber diameter at higher CuO-GO loading. The thermal-crosslinked nanofibrous mats facilitated a controlled and sustained swelling and degradation profile, with negligible compromise in the mechanical integrity of the mats. Enhanced swelling behavior was observed, which is advantageous for efficient exudate uptake in wound environments. The mats demonstrated thermal stability and retained their physicochemical properties post-autoclave sterilization. *In vitro* assays confirmed excellent cytocompatibility and hemocompatibility while *in vivo* evaluations corroborated their therapeutic potential for biomedical applications. It's ability to rapidly restore tissue integrity while minimizing scarring

View Article Online
DOI: 10.1039/D5MA01301A

presents an advantage over traditional gauze or hydrogel dressings. The streamlined electrospinning process, combined with inherent biocompatibility and the ability to conform to complex wound topographies, spotlight nanofibrous mats as a premier candidate for translational research and industrial mass production for clinical applications.

Declaration of Competing Interest

The authors declare that they have no known competing financial interests or personal relationships that could have appeared to influence the work reported in this paper.

Acknowledgement

M. N. Khan is grateful to the Centennial Research Grant (CRG), University of Dhaka, Bangladesh (ref No. Reg/Admin-3/47874) for funding support. The authors thank the Ministry of Education, Bangladesh (grant no. SD20221995) under the Higher Education Research Project (BANBEIS, Dhaka). M. A. Hasnat thanks NST fellowship from the Ministry of Science and Technology, Bangladesh. R.S. thanks the PhD fellowship from the Higher Education Research Project.

REFERENCES

[1] P. Squinca *et al.*, "Multifunctional Ginger Nanofiber Hydrogels with Tunable Absorption: The Potential for Advanced Wound Dressing Applications," *Biomacromolecules*, vol. 22, no. 8, pp. 3202–3215, Aug. 2021, doi: 10.1021/acs.biomac.1c00215.

[2] L. Chen, J. Min, and F. Wang, "Copper homeostasis and cuproptosis in health and disease," *Signal Transduct. Target. Ther.*, vol. 7, no. 1, 2022, doi: 10.1038/s41392-022-01229-y.

[3] W. Zhou, L. Zi, Y. Cen, C. You, and M. Tian, "Copper Sulfide Nanoparticles-

View Article Online
DOI: 10.1039/D5MA01301A

Incorporated Hyaluronic Acid Injectable Hydrogel With Enhanced Angiogenesis to Promote Wound Healing," *Front. Bioeng. Biotechnol.*, vol. 8, May 2020, doi: 10.3389/fbioe.2020.00417.

[4] Z. Zhang *et al.*, "Copper incorporated biomaterial-based technologies for multifunctional wound repair.," *Theranostics*, vol. 14, no. 2, pp. 547–570, 2024, doi: 10.7150/thno.87193.

[5] E. Melamed, P. Kiambi, D. Okoth, I. Honigber, E. Tamir, and G. Borkow, "Healing of Chronic Wounds by Copper Oxide-Impregnated Wound Dressings-Case Series.," *Medicina (Kaunas).*, vol. 57, no. 3, p. 296, Mar. 2021, doi: 10.3390/medicina57030296.

[6] M. Soliman, A. A. Sadek, H. N. Abdelhamid, and K. Hussein, "Graphene oxide-cellulose nanocomposite accelerates skin wound healing," *Res. Vet. Sci.*, vol. 137, no. May, pp. 262–273, 2021, doi: 10.1016/j.rvsc.2021.05.013.

[7] W. Fadhil, I. Jabbar, E. Ali, G. Sulaiman, R. Khan, and H. Mohammed, "Freshly Prepared Graphene Oxide Nanoparticles' Wound-Healing Potential and Antibacterial Activity Specifically Against Staphylococcus aureus: In Vivo Efficacy and Clinical Isolate Evaluation," *Plasmonics*, pp. 0.1007/s11468-024, 2024, doi: 10.1007/s11468-024-02296-3.

[8] G.-M. Lanno *et al.*, "Antibacterial Porous Electrospun Fibers as Skin Scaffolds for Wound Healing Applications," *ACS Omega*, vol. 5, no. 46, pp. 30011–30022, Nov. 2020, doi: 10.1021/acsomega.0c04402.

[9] C. Cui, S. Sun, S. Wu, S. Chen, J. Ma, and F. Zhou, "Electrospun chitosan nanofibers for wound healing application," *Eng. Regen.*, vol. 2, pp. 82–90, 2021, doi: https://doi.org/10.1016/j.engreg.2021.08.001.

View Article Online
DOI: 10.1039/D5MA01301A

[10] T. Siddike Moin, M. Rani Sarkar, M. F. Mahmud Chowdhury, M. M. Rahman, and M. N. Khan, "Electrospun Poly(vinyl alcohol)/Chitosan Nanofibers Embedded with a CuO–GO Nanocomposite for pH-Sensitive Adsorption of Heavy Metal Ions and Organic Dyes," *ACS Omega*, vol. 10, no. 19, pp. 19294–19313, May 2025, doi: 10.1021/acsomega.4c08836.

[11] P. Sagitha, C. R. Reshmi, S. P. Sundaran, and A. Sujith, "Recent advances in post-modification strategies of polymeric electrospun membranes," *Eur. Polym. J.*, vol. 105, pp. 227–249, Aug. 2018, doi: 10.1016/J.EURPOLYMJ.2018.05.033.

[12] S. Sandra *et al.*, "Synthesis of electrospun PVA/chitosan nanofibrous scaffold impregnated with CuO nanoparticles for wound healing," *Cellulose*, vol. 31, no. 10, pp. 6387–6401, 2024, doi: 10.1007/s10570-024-05960-3.

[13] E. Ghasemian Lemraski *et al.*, "Antimicrobial Double-Layer Wound Dressing Based on Chitosan/Polyvinyl Alcohol/Copper: In vitro and in vivo Assessment.," *Int. J. Nanomedicine*, vol. 16, pp. 223–235, Jan. 2021, doi: 10.2147/IJN.S266692.

[14] M. Heidari, S. H. Bahrami, M. Ranjbar-Mohammadi, and P. B. Milan, "Smart electrospun nanofibers containing PCL/gelatin/graphene oxide for application in nerve tissue engineering," *Mater. Sci. Eng. C*, vol. 103, no. July 2018, p. 109768, Oct. 2019, doi: 10.1016/j.msec.2019.109768.

[15] P. Dubey and P. Gopinath, "PEGylated graphene oxide-based nanocomposite-grafted chitosan/polyvinyl alcohol nanofiber as an advanced antibacterial wound dressing," *RSC Adv.*, vol. 6, no. 73, pp. 69103–69116, 2016, doi: 10.1039/C6RA12192F.

[16] I. H. Ali *et al.*, "Antimicrobial and Wound-Healing Activities of Graphene-Reinforced

View Article Online
DOI: 10.1039/D5MA01301A

Electrospun Chitosan/Gelatin Nanofibrous Nanocomposite Scaffolds," *ACS Omega*, vol. 7, no. 2, pp. 1838–1850, Jan. 2022, doi: 10.1021/acsomega.1c05095.

[17] K. S. Venkataprasanna *et al.*, "Fabrication of Chitosan/PVA/GO/CuO patch for potential wound healing application," *Int. J. Biol. Macromol.*, vol. 143, pp. 744–762, Jan. 2020, doi: 10.1016/j.ijbiomac.2019.10.029.

[18] T. Jayaramudu *et al.*, "Chitosan capped copper oxide/copper nanoparticles encapsulated microbial resistant nanocomposite films," *Int. J. Biol. Macromol.*, vol. 128, pp. 499–508, May 2019, doi: 10.1016/j.ijbiomac.2019.01.145.

[19] W. S. J. Hummers and R. E. Offeman, "Preparation of Graphitic Oxide," *J. Am. Chem. Soc.*, vol. 80, no. 6, p. 1339, Mar. 1958, doi: 10.1021/ja01539a017.

[20] M. S. Enayati *et al.*, "Crystallinity study of electrospun poly (vinyl alcohol) nanofibers: effect of electrospinning, filler incorporation, and heat treatment," *Iran. Polym. J. (English Ed.*, vol. 25, no. 7, pp. 647–659, 2016, doi: 10.1007/s13726-016-0455-3.

[21] K. Selatile, S. S. Ray, V. Ojijo, and R. E. Sadiku, "Morphological, Thermal, and Mechanical Properties of Electrospun Recycled Poly(ethylene terephthalate)/Graphene Oxide Composite Nanofiber Membranes," *ACS Omega*, vol. 6, no. 32, pp. 21005–21015, Aug. 2021, doi: 10.1021/acsomega.1c02578.

[22] A. Moradi, S. Pramanik, F. Ataollahi, T. Kamarul, and B. Pingguan-Murphy, "Archimedes revisited: computer assisted micro-volumetric modification of the liquid displacement method for porosity measurement of highly porous light materials," *Anal. Methods*, vol. 6, no. 12, pp. 4396–4401, 2014, doi: 10.1039/C4AY00666F.

View Article Online
DOI: 10.1039/D5MA01301A

[23] S. S. Karim, S. Farrukh, A. Hussain, M. Younas, and T. Noor, "The influence of polymer concentration on the morphology and mechanical properties of asymmetric polyvinyl alcohol (PVA) membrane for O 2 /N 2 separation," *Polym. Polym. Compos.*, vol. 30, p. 09673911221090053, Jan. 2022, doi: 10.1177/09673911221090053.

[24] M. Golandi, J. Mova, F. S. Ahmadi, and F. Kalalinia, "Improvement of the Wound-Healing Process by Curcumin-Loaded Chitosan / Collagen Blend Electrospun Nano fi bers : In Vitro and In Vivo Studies," 2021, doi: 10.1021/acsbiomaterials.1c00131.

[25] X. Y. Jia *et al.*, "Dynamically Cross-Linked Double-Network Hydrogels with Matched Mechanical Properties and Ideal Biocompatibility for Artificial Blood Vessels," *ACS Appl. Mater. Interfaces*, vol. 16, no. 22, pp. 28134–28146, Jun. 2024, doi: 10.1021/acsami.4c03063.

[26] X. Jia *et al.*, "Hydrophobic aerogel-modified hemostatic gauze with thermal management performance.," *Bioact. Mater.*, vol. 26, pp. 142–158, Aug. 2023, doi: 10.1016/j.bioactmat.2023.02.017.

[27] L. Guo *et al.*, "Optimal H2O2 preconditioning to improve bone marrow mesenchymal stem cells' engraftment in wound healing," *Stem Cell Res. Ther.*, vol. 11, no. 1, p. 434, 2020, doi: 10.1186/s13287-020-01910-5.

[28] M. van de Vyver *et al.*, "Histology Scoring System for Murine Cutaneous Wounds.," *Stem Cells Dev.*, vol. 30, no. 23, pp. 1141–1152, Dec. 2021, doi: 10.1089/scd.2021.0124.

[29] S. Khan *et al.*, "Comparative Evaluation of Masson's Trichrome and Picrosirius Red Staining for Digital Collagen Quantification Using ImageJ in Rabbit Wound Healing Research," *J. Exp. Biol. Agric. Sci.*, vol. 11, pp. 822–833, 2023, doi:

View Article Online
DOI: 10.1039/D5MA01301A

10.18006/2023.11(5).822.833.

[30] T. Siddike Moin, M. M. Rani Sarkar, Mukta; Mahmud Chowdhury, Mohammed Farhad ; Rahman, and M. N. Khan, "Electrospun Polyvinyl alcohol/Chitosan Nanofibers embedded with CuO-GO nanocomposite for pH-sensitive adsorption of Heavy Metal ions and Organic Dyes," *ACS Omega*, 2025, doi: doi.org/10.1021/acsomega.4c08836.

[31] A. M. Dimiev and J. M. Tour, "Mechanism of Graphene Oxide Formation," *ACS Nano*, vol. 8, no. 3, pp. 3060–3068, Mar. 2014, doi: 10.1021/nn500606a.

[32] S. R. Kiran Kumar *et al.*, "Highly efficient multipurpose graphene oxide embedded with copper oxide nanohybrid for electrochemical sensors and biomedical applications," *J. Sci. Adv. Mater. Devices*, vol. 2, no. 4, pp. 493–500, Dec. 2017, doi: 10.1016/j.jsamd.2017.08.003.

[33] D. C. Marcano *et al.*, "Improved Synthesis of Graphene Oxide," *ACS Nano*, vol. 4, no. 8, pp. 4806–4814, Aug. 2010, doi: 10.1021/nn1006368.

[34] H. A. Sarode, D. P. Barai, B. A. Bhanvase, R. P. Ugwekar, and V. Saharan, "Investigation on preparation of graphene oxide-CuO nanocomposite based nanofluids with the aid of ultrasound assisted method for intensified heat transfer properties," *Mater. Chem. Phys.*, vol. 251, no. August 2019, p. 123102, Sep. 2020, doi: 10.1016/j.matchemphys.2020.123102.

[35] O. Messaoudi *et al.*, "Annealing temperature investigation on electrodeposited Cu2O properties," *Phase Transitions*, vol. 93, no. 10–11, pp. 1089–1099, Nov. 2020, doi: 10.1080/01411594.2020.1837379.

View Article Online
DOI: 10.1039/D5MA01301A

[36] M. Guzman, M. Arcos, J. Dille, C. Rousse, S. Godet, and L. Malet, "Effect of the Concentration and the Type of Dispersant on the Synthesis of Copper Oxide Nanoparticles and Their Potential Antimicrobial Applications," *ACS Omega*, vol. 6, no. 29, pp. 18576–18590, Jul. 2021, doi: 10.1021/acsomega.1c00818.

[37] R. K. Singh Rathour, J. Bhattacharya, and A. Mukherjee, "Facile Synthesis of Graphene Oxide for Multicycle Adsorption of Aqueous Pb2+ in the Presence of Divalent Cations and Polyatomic Anions," *J. Chem. Eng. Data*, vol. 63, no. 9, pp. 3465–3474, Sep. 2018, doi: 10.1021/acs.jced.8b00344.

[38] K. V Ragavan and N. K. Rastogi, "Graphene–copper oxide nanocomposite with intrinsic peroxidase activity for enhancement of chemiluminescence signals and its application for detection of Bisphenol-A," *Sensors Actuators B Chem.*, vol. 229, pp. 570–580, 2016, doi: https://doi.org/10.1016/j.snb.2016.02.017.

[39] C. Mellado, T. Figueroa, R. Baez, M. Meléndrez, and K. Fernández, "Effects of probe and bath ultrasonic treatments on graphene oxide structure," *Mater. Today Chem.*, vol. 13, pp. 1–7, Sep. 2019, doi: 10.1016/j.mtchem.2019.04.006.

[40] S. P. Chawla, S. R. Kanatt, and A. K. Sharma, "Chitosan," in *Polysaccharides*, K. G. Ramawat and J.-M. Mérillon, Eds., Cham: Springer International Publishing, 2015, pp. 219–246. doi: 10.1007/978-3-319-16298-0_13.

[41] M. P. Weir *et al.*, "Distortion of Chain Conformation and Reduced Entanglement in Polymer–Graphene Oxide Nanocomposites," *ACS Macro Lett.*, vol. 5, no. 4, pp. 430–434, Apr. 2016, doi: 10.1021/acsmacrolett.6b00100.

[42] E. Van Etten, E. Ximenes, L. Tarasconi, I. Garcia, M. M. Forte, and H. Boudinov,

View Article Online
DOI: 10.1039/D5MA01301A

"Insulating characteristics of polyvinyl alcohol for integrated electronics," *Thin Solid Films*, vol. 568, pp. 111–116, 2014, doi: 10.1016/j.tsf.2014.07.051.

[43] S. A. Mathew and S. Arumainathan, "Crosslinked Chitosan–Gelatin Biocompatible Nanocomposite as a Neuro Drug Carrier," *ACS Omega*, vol. 7, no. 22, pp. 18732–18744, Jun. 2022, doi: 10.1021/acsomega.2c01443.

[44] G. Wu, J. Zhang, X. Wan, Y. Yang, and S. Jiang, "Chitosan-based biopolysaccharide proton conductors for synaptic transistors on paper substrates," *J. Mater. Chem. C*, vol. 2, no. 31, pp. 6249–6255, 2014, doi: 10.1039/C4TC00652F.

[45] R. Eivazzadeh-Keihan *et al.*, "Effective Combination of rGO and CuO Nanomaterials through Poly(p-phenylenediamine) Texture: Utilizing It as an Excellent Supercapacitor," *Energy and Fuels*, vol. 35, no. 13, pp. 10869–10877, Jul. 2021, doi: 10.1021/acs.energyfuels.1c01132.

[46] A. Haider, S. Haider, and I.-K. Kang, "A comprehensive review summarizing the effect of electrospinning parameters and potential applications of nanofibers in biomedical and biotechnology," *Arab. J. Chem.*, vol. 11, no. 8, pp. 1165–1188, 2018, doi: https://doi.org/10.1016/j.arabjc.2015.11.015.

[47] A. A. Amer, R. S. Mohammed, Y. Hussein, A. S. M. Ali, and A. A. Khalil, "Development of Lepidium sativum Extracts/PVA Electrospun Nanofibers as Wound Healing Dressing," *ACS Omega*, vol. 7, no. 24, pp. 20683–20695, Jun. 2022, doi: 10.1021/acsomega.2c00912.

[48] F. E. Mustafa and B.-K. Lee, "Improved Mechanical Stability and Regulated Gentamicin-Release of Polyvinyl Alcohol/Chitosan Nanofiber Membranes via Heat Treatment," *J. Biomed. Mater. Res. Part A*, vol. 113, no. 4, p. e37905, 2025, doi:

View Article Online
DOI: 10.1039/D5MA01301A

https://doi.org/10.1002/jbm.a.37905.

[49] Y. Cheng *et al.*, "Exploring the potential of a polyvinyl alcohol/chitosan-based nanofibrous matrix for erythromycin delivery: fabrication, in vitro and in vivo evaluation," *RSC Adv.*, vol. 13[1] S. P, no. 27, pp. 18450–18460, 2023, doi: 10.1039/D3RA02987E.

[50] H. Zhang, L. Lin, L. Ren, Y. Liu, and R. Song, "Characterization of CS/PVA/GO electrospun nanofiber membrane with astaxanthin," *J. Appl. Polym. Sci.*, vol. 138, no. 14, p. 50166, 2021, doi: https://doi.org/10.1002/app.50166.

[51] L. Cao, F. Zhang, Q. Wang, and X. Wu, "Fabrication of chitosan/graphene oxide polymer nanofiber and its biocompatibility for cartilage tissue engineering," *Mater. Sci. Eng. C*, vol. 79, pp. 697–701, 2017, doi: 10.1016/j.msec.2017.05.056.

[52] H. Mahmoodi, M. Fattahi, and M. Motevassel, "Graphene oxide–chitosan hydrogel for adsorptive removal of diclofenac from aqueous solution: preparation{,} characterization{,} kinetic and thermodynamic modelling," *RSC Adv.*, vol. 11, no. 57, pp. 36289–36304, 2021, doi: 10.1039/D1RA06069D.

[53] P.-P. Zuo *et al.*, "Fabrication of biocompatible and mechanically reinforced graphene oxide-chitosan nanocomposite films," *Chem. Cent. J.*, vol. 7, p. 39, 2013, doi: 10.1186/1752-153X-7-39.

[54] J. Kulczyńska *et al.*, "Sustainable poly(vinyl alcohol)/chitosan electrospun nanofibers and casted films with bioactive additives – comparative study on physicochemical properties and in vitro biological activity," *Ind. Crops Prod.*, vol. 233, p. 121335, 2025, doi: https://doi.org/10.1016/j.indcrop.2025.121335.

View Article Online
DOI: 10.1039/D5MA01301A

[55] M. Y. Elnaggar, E. S. Fathy, and L. A. Wahab, "Performance relative study of metal oxide nanoparticles on mechanical, thermal, and optical characteristics of gamma-irradiated poly (vinyl alcohol) nanocomposites," *Appl. Organomet. Chem.*, vol. 37, no. 2, 2023, doi: 10.1002/aoc.6965.

[56] P. Mandal, K. Stokes, G. Hernández, D. Brandell, and J. Mindemark, "Influence of Binder Crystallinity on the Performance of Si Electrodes with Poly(vinyl alcohol) Binders," *ACS Appl. Energy Mater.*, vol. 4, no. 4, pp. 3008–3016, 2021, doi: 10.1021/acsaem.0c02051.

[57] N. Narayanan *et al.*, "Harnessing Fiber Diameter-Dependent Effects of Myoblasts Toward Biomimetic Scaffold-Based Skeletal Muscle Regeneration," *Front. Bioeng. Biotechnol.*, vol. Volume 8-, 2020, doi: 10.3389/fbioe.2020.00203.

[58] S. Yao, Y. Li, Z. Zhou, and H. Yan, "Graphene oxide-assisted preparation of poly(vinyl alcohol)/carbon nanotube/reduced graphene oxide nanofibers with high carbon content by electrospinning technology," *RSC Adv.*, vol. 5, no. 111, pp. 91878–91887, 2015, doi: 10.1039/c5ra15985g.

[59] K. Kusjuriansah *et al.*, "Composite Hydrogel of Poly(vinyl alcohol) Loaded by Citrus hystrix Leaf Extract, Chitosan, and Sodium Alginate with In Vitro Antibacterial and Release Test," *ACS Omega*, vol. 9, no. 11, pp. 13306–13322, Mar. 2024, doi: 10.1021/acsomega.3c10143.

[60] H. M. Alghamdi and A. Rajeh, "Synthesis and improved optical, electrical, and dielectric properties of PEO/PVA/CuCo2O4 nanocomposites," *Sci. Rep.*, vol. 14, no. 1, p. 18925, 2024, doi: 10.1038/s41598-024-69982-4.

[61] L. Liu, J. Zhang, J. Zhao, and F. Liu, "Mechanical properties of graphene oxides,"

View Article Online
DOI: 10.1039/D5MA01301A

Nanoscale, vol. 4, no. 19, pp. 5910–5916, 2012, doi: 10.1039/C2NR31164J.

[62] L. Shao, X. Chang, Y. Zhang, Y. Huang, Y. Yao, and Z. Guo, "Graphene oxide cross-linked chitosan nanocomposite membrane," *Appl. Surf. Sci.*, vol. 280, pp. 989–992, 2013, doi: https://doi.org/10.1016/j.apsusc.2013.04.112.

[63] C. Wang, C.-W. Tsai, and T. Hashimoto, "Poly(vinyl alcohol) Fibrils with Highly Oriented Amorphous Chains Developed in Electrospun Nanofibers," *Macromolecules*, vol. 57, no. 5, pp. 2191–2204, Mar. 2024, doi: 10.1021/acs.macromol.3c02047.

[64] B. Wang *et al.*, "Colloids and Surfaces A : Physicochemical and Engineering Aspects Fabrication of PVA / graphene oxide / TiO 2 composite nanofibers through electrospinning and interface sol – gel reaction : Effect of graphene oxide on PVA nanofibers and growth of TiO 2," *Colloids Surfaces A Physicochem. Eng. Asp.*, vol. 457, pp. 318–325, 2014, doi: 10.1016/j.colsurfa.2014.06.006.

[65] S. Szunerits *et al.*, "Biosensors integrated within wearable devices for monitoring chronic wound status," *APL Bioeng.*, vol. 9, no. 1, p. 10901, 2025, doi: 10.1063/5.0220516.

[66] A. Eskandarinia *et al.*, "A Novel Bilayer Wound Dressing Composed of a Dense Polyurethane/Propolis Membrane and a Biodegradable Polycaprolactone/Gelatin Nanofibrous Scaffold.," *Sci. Rep.*, vol. 10, no. 1, p. 3063, Feb. 2020, doi: 10.1038/s41598-020-59931-2.

[67] M. Gozutok, V. Sadhu, and H. T. Sasmazel, "Development of Poly(vinyl alcohol) (PVA)/Reduced Graphene Oxide (rGO) Electrospun Mats," *J. Nanosci. Nanotechnol.*, vol. 19, no. 7, pp. 4292–4298, 2019, doi: 10.1166/jnn.2019.16290.

View Article Online
DOI: 10.1039/D5MA01301A

[68] A. Parvinnasab, S. Shahroudi, E. Salahinejad, A. H. Taghvaei, S. A. Sharifi Fard, and E. Sharifi, "Antibacterial nanofibrous wound dressing mats made from blended chitosan-copper complexes and polyvinyl alcohol (PVA) using electrospinning," *Carbohydr. Polym. Technol. Appl.*, vol. 8, p. 100564, 2024, doi: https://doi.org/10.1016/j.carpta.2024.100564.

[69] R. Liu, X. Xu, X. Zhuang, and B. Cheng, "Solution blowing of chitosan/PVA hydrogel nanofiber mats," *Carbohydr. Polym.*, vol. 101, no. 1, pp. 1116–1121, 2014, doi: 10.1016/j.carbpol.2013.10.056.

[70] C. L. Huang, S. Y. Peng, Y. J. Wang, W. C. Chen, and J. H. Lin, "Microstructure and characterization of electrospun poly(vinyl alcohol) nanofiber scaffolds filled with graphene nanosheets," *J. Appl. Polym. Sci.*, vol. 132, no. 17, pp. 1–11, 2015, doi: 10.1002/app.41891.

[71] R. de S. Victor, D. dos S. Gomes, A. M. da C. Santos, S. M. Torres, G. de A. Neves, and R. R. Menezes, "3D nanofibrous structures formed of high content chitosan/PVA and chitosan/PLA blends using air-heated solution blow spinning (A-HSBS)," *J. Mater. Sci.*, vol. 59, no. 35, pp. 16768–16788, Sep. 2024, doi: 10.1007/s10853-024-10121-9.

[72] T. Hasan Aneem, S. O. Firdous, A. Anjum, S. Y. Wong, X. Li, and M. T. Arafat, "Enhanced wound healing of ciprofloxacin incorporated PVA/alginate/PAA electrospun nanofibers with antibacterial effects and controlled drug release," *Mater. Today Commun.*, vol. 38, no. December 2023, 2024, doi: 10.1016/j.mtcomm.2023.107950.

[73] K. Wang *et al.*, "Biocompatibility of Graphene Oxide.," *Nanoscale Res. Lett.*, vol. 6, no. 1, p. 8, Dec. 2011, doi: 10.1007/s11671-010-9751-6.

View Article Online
DOI: 10.1039/D5MA01301A

[74] P. Bhattacharya, S. Swarnakar, S. Ghosh, S. Majumdar, and S. Banerjee, "Disinfection of drinking water via algae mediated green synthesized copper oxide nanoparticles and its toxicity evaluation," *J. Environ. Chem. Eng.*, vol. 7, no. 1, p. 102867, 2019, doi: 10.1016/j.jece.2018.102867.

[75] B. K. Gu, S. J. Park, M. S. Kim, C. M. Kang, J.-I. Kim, and C.-H. Kim, "Fabrication of sonicated chitosan nanofiber mat with enlarged porosity for use as hemostatic materials," *Carbohydr. Polym.*, vol. 97, no. 1, pp. 65–73, 2013, doi: https://doi.org/10.1016/j.carbpol.2013.04.060.

[76] K. Quan, G. Li, D. Luan, Q. Yuan, L. Tao, and X. Wang, "Black hemostatic sponge based on facile prepared cross-linked graphene," *Colloids Surfaces B Biointerfaces*, vol. 132, pp. 27–33, 2015, doi: https://doi.org/10.1016/j.colsurfb.2015.04.067.

[77] S. Eslaminezhad, F. Moradi, and M. R. Hojjati, "Evaluation of the wound healing efficacy of new antibacterial polymeric nanofiber based on polyethylene oxide coated with copper nanoparticles and defensin peptide: An in-vitro to in-vivo assessment," *Heliyon*, vol. 10, no. 8, p. e29542, 2024, doi: https://doi.org/10.1016/j.heliyon.2024.e29542.

[78] S. Faisal *et al.*, "In Vivo Analgesic, Anti-Inflammatory, and Anti-Diabetic Screening of Bacopa monnieri -Synthesized Copper Oxide Nanoparticles," *ACS Omega*, vol. 7, no. 5, pp. 4071–4082, Feb. 2022, doi: 10.1021/acsomega.1c05410.

[79] L. Qi *et al.*, "Guiding the Path to Healing: CuO 2 -Laden Nanocomposite Membrane for Diabetic Wound Treatment," *Small*, vol. 20, no. 3, p. 2305100, Jan. 2024, doi: 10.1002/smll.202305100.

[80] F. Back *et al.*, "Platelet Extracellular Vesicles Loaded Gelatine Hydrogels for Wound

View Article Online
DOI: 10.1039/D5MA01301A

Care.," *Adv. Healthc. Mater.*, vol. 14, no. 1, p. e2401914, Jan. 2025, doi: 10.1002/adhm.202401914.

[81] A. P. Kornblatt, V. G. Nicoletti, and A. Travaglia, "The neglected role of copper ions in wound healing," *J. Inorg. Biochem.*, vol. 161, pp. 1–8, 2016, doi: 10.1016/j.jinorgbio.2016.02.012.

[82] H. Hodaei, Z. Esmaeili, Y. Erfani, S. S. Esnaashari, M. Geravand, and M. Adabi, "Preparation of biocompatible Zein/Gelatin/Chitosan/PVA based nanofibers loaded with vitamin E-TPGS via dual-opposite electrospinning method," *Sci. Rep.*, vol. 14, no. 1, p. 23796, 2024, doi: 10.1038/s41598-024-74865-9.

[83] B. Farrugia *et al.*, "Chitosan-Based Heparan Sulfate Mimetics Promote Epidermal Formation in a Human Organotypic Skin Model," *Adv. Funct. Mater.*, vol. 28, p. 1802818, Sep. 2018, doi: 10.1002/adfm.201802818.

[84] R. Feng, Y. Yu, C. Shen, Y. Jiao, and C. Zhou, "Impact of graphene oxide on the structure and function of important multiple blood components by a dose-dependent pattern.," *J. Biomed. Mater. Res. A*, vol. 103, no. 6, pp. 2006–2014, Jun. 2015, doi: 10.1002/jbm.a.35341.

[85] K. H. Hussein, H. N. Abdelhamid, X. Zou, and H.-M. Woo, "Ultrasonicated graphene oxide enhances bone and skin wound regeneration," *Mater. Sci. Eng. C*, vol. 94, pp. 484–492, 2019, doi: https://doi.org/10.1016/j.msec.2018.09.051.

[86] J. Li *et al.*, "N-acetyl cysteine-loaded graphene oxide-collagen hybrid membrane for scarless wound healing.," *Theranostics*, vol. 9, no. 20, pp. 5839–5853, 2019, doi: 10.7150/thno.34480.

View Article Online
DOI: 10.1039/D5MA01301A

[87] M. E. Astaneh and N. Fereydouni, “Advancing diabetic wound care: The role of copper-containing hydrogels.,” *Heliyon*, vol. 10, no. 20, p. e38481, Oct. 2024, doi: 10.1016/j.heliyon.2024.e38481.

View Article Online
DOI: 10.1039/D5MA01301A

View Article Online
DOI: 10.1039/D5MA01301A

Data availability statements

The data supporting this article have been included as part of the Supplementary Information.